University of Twente

EEMCS / Electrical Engineering
Robotics and *Mechatronics*

Ultrasound-guided control of a Minimally-Invasive Surgical instrument

T.T.M. (Tim) Ellenbroek

MSc Report

Committee:
Prof.dr.ir. S. Stramigioli
Dr. S. Misra
R.J. Roesthuis, MSc
G.J. Vrooijink, MSc
Ir. E.E.G. Hekman

September 2013

Report nr. 025RAM2013
Robotics and Mechatronics
EE-Math-CS
University of Twente
P.O. Box 217
7500 AE Enschede
The Netherlands

Abstract

Development in Minimally Invasive Surgery (MIS) aims at minimizing patient trauma. A major improvement in cardiac surgery with respect to minimizing patient trauma would be omitting the need to perform a sternotomy. Working around the sternum, the surgeon needs instruments that perform a task inside the body while the controls are outside the body. Images should also be recorded inside the body, but shown to the surgeon outside the body. Amongst others, ultrasound, Magnetic Resonance Imaging (MRI) and Computed Tomography (CT) are imaging modalities that would fit in an MIS environment. MRI has the disadvantage that not many instruments are suited for the applied magnetic fields, and CT has the disadvantage of radiation. Both MRI and CT are also expensive imaging modalities. Therefore, ultrasound is chosen to provide images in this project.

Instruments allowing the surgeon to operate from outside the body are generalized in the family of MIS instruments. These instruments allow the surgeon to operate through small incisions, while the instrument performs the task at the target location inside the body. The MIS instrument used in this project is a cylinder-shaped device, of the family of continuum robots, that has a flexible tip. The tip is actuated by pulling on two sets of tendons that emerge from the rear of the instrument.

The MIS instrument is mounted in an experimental setup, where two motors operate the instrument's tendons. The instrument is mounted on a linear stage, allowing for movement along its longitudinal axis. A 2D ultrasound probe is positioned above the tip to visualize it. Image processing is used to find the tip location from the ultrasound images and the measured position is used for closed-loop control. The setup and instrument are characterized and a number of (model-based) controllers are designed and evaluated.

Acknowledgements

The successful completion of my MSc. project has been made possibly with the help of quite a few people. Many thanks to anyone involved in that process, but I would like to thank some people in particular.

I would like to thank my thesis supervisor, Dr. Sarthak Misra, for the opportunity to work in the Medical Robotics team. The project has been challenging on engineering, academic and personal level. I would like to thank Ir. Edsko Hekman for his advice on the mechanical design of the experiment setup. Thanks to Jules Scheltes, who helped me with the instrument. Thanks to the people of the RaM group, who have helped arranging a lot along the way and in completing the project.

I sincerely thank my daily supervisor Roy Roesthuis MSc., specifically for his help on modelling. I sincerely thank my daily supervisor Guus Vrooijink MSc., specifically for his help with the software framework and development of image processing software that has been used throughout this project.

I thank my fellow medical robotics students for their help and support and for making the lab a nice place to work.

Last, but definitely not least, I would like to thank my family and my girlfriend Wendy, for their unlimited support during my academic career and the MSc. project. Without your support, I would not have been able to achieve all this.

Many, many thanks!

— Tim Ellenbroek

Contents

Introduction

The past few decades have shown a change in surgery: open surgery is replaced by procedures using endoscopic or laparoscopic instruments. The number of surgical procedures using this equipment has increased over the past decades. The field concerned with -amongst others- these techniques is called Minimally Invasive Surgery (MIS). In short, MIS focusses on minimizing patient trauma. For example, 'open' surgical procedures are replaced by keyhole surgery, which only requires small incisions. Therefore patients recover faster from keyhole surgery than from open surgery.

MIS requires novel tools, such as laparoscopic instruments or endoscopic instruments. Robotic instruments have also been introduced. The most familiar example is the *da Vinci*© Surgical System (*da Vinci*© Surgical Systems, Intuitive Surgical®, Sunnyvale, California, USA), shown in figure 1.

Figure 1: The *da Vinci*© Surgical System. Image courtesy of Intuitive Surgical® Inc. (Intuitive Surgical Inc., 2013).

Not only the surgeon's tools have evolved towards minimally invasive methods, also the imaging modalities have evolved in that direction. A few decades ago, a surgeon would have to open up a patient to be able to inspect the internal organs. Pinhole endoscopic camera's have reduced patient trauma for these situations, only requiring small cuts. These days, imaging modalities like Ultrasound, Computed Tomography (CT), Magnetic Resonance Imaging (MRI) are also available.

When focussing on cardiac surgery, the ultimate goal is to be able to perform surgery while the heart keeps beating. This would overcome the risks involved with temporarily stopping the heart [1]. However, in some procedures stopping the heartbeat is inevitable, for example in Transapical Aortic Valve Implantation (TAVI). In TAVI an artificial valve is implanted, where surgeons need to induce cardiac arrest in order to keep the valve from moving. Although the heartbeat is stopped, respiratory motion remains [2]. Accuracy of placement could be improved, or the time to complete the procedure could be reduced, if a robotic instrument would take over the surgeon's task of compensating for the respiratory motion.

Kesner et al. worked on compensation techniques for motion in the direction of the longitudinal axis of cardiac catheters, and indicate that "future work will be required to extend this motion compensation technology to cardiac surgery applications that require additional DOF for end effector positioning" [3].

The above considerations lead to the research goal of this project for the use of a prototype laparoscopical minimally invasive surgical instrument. The instrument tip will be controlled in the plane perpendicular to the longitudinal axis of the instrument. Ultrasound imaging modality is chosen to measure the position of the instrument tip, which will be used for control.

Contributions

During the work on this project, contributions to the research field have been made. The work done is:

- An integrated system is developed that allows the user to explore the possibilities of an instrument or imaging modality for cardiac interventions.
- The integrated system, using some non-conventional design decisions, allowed for exploratory research on the design considerations for future use in a clinical environment.
- Augmentations are made to existing modelling techniques for flexible instruments.
- Control algorithms are evaluated that improve the accuracy in a range suitable for the clinical application.

Thesis Outline

Part 1 introduces the reader to conceptual and design considerations for the experimental setup, called: Platform for Laparoscopically Actuated-Tip Instrument usiNg Ultrasound-image Modality (PLATINUM). Part 2 introduces a model that describes the behaviour of the instrument. Part 3 uses that model in control. Some different control strategies will be explained. Part 4 describes experimental results for these control strategies. The sections Conclusions and Recommendations and Future Work summarize the results and look for opportunities to improve the results in the future.

Thesis Contributions

[1] G.J. Vrooijink, T.T.M. Ellenbroek and S. Misra, "A Preliminary Study on using a Robotically-Actuated Delivery Sheath (RADS) for Transapical Aortic Valve Implantation", In *Proceedings of the IEEE International Conferance on Robotics and Automation (ICRA) 2014*, Hong-Kong, China, May-June 2014. in preparation.

Part I

‘Platform for Laparoscopically Actuated-Tip Instrument usiNg Ultrasound-image Modality’

Platform for Laparoscopically Actuated-Tip Instrument usiNg Ultrasound-image Modality

Tim T.M. Ellenbroek, Gustaaf J. Vrooijink, Roy J. Roesthuis and Sarthak Misra
University of Twente, The Netherlands

Abstract— **This article describes the design and construction of the Platform for Laparoscopically Actuated-Tip Instrument usiNg Ultrasound-image Modality (PLATINUM). This setup provides means to operate a surgical instrument of the continuum robot class and acquire feedback via ultrasound images.**

I. SURGICAL INSTRUMENT

The surgical instrument around which the setup will be constructed is a prototype constructed by DEAM (DEAM corporation, Amsterdam, The Netherlands) and is depicted in figure 1. The instrument is based on the construction explained by Breedveld [1]. The instrument belongs to the family of continuum robots: devices that bend with a continuous curvature.

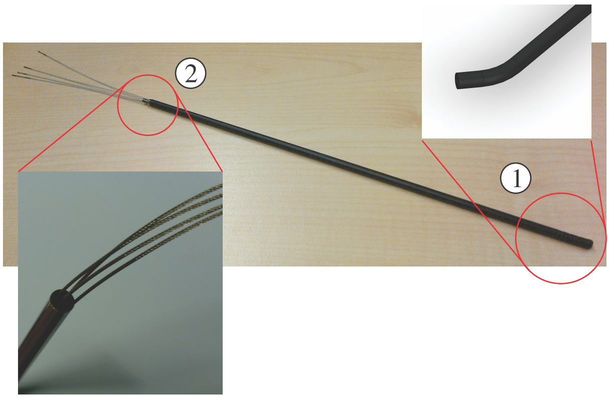

Fig. 1. Laparoscopical surgical instrument. The tip of this cylinder ① is flexible and can be bent by pulling on the tendons (wires) at the rear of the instrument ②. Two degrees of freedom can be controlled using two pairs of antagonistic tendons.

A. *Modifications*

The instrument is modified to prevent tendons getting tangled up and to make the instrument water-proof. The part of the inner spring running through the rigid cylinder is taken out, and 8 excess tendons are cut behind the tip. To prevent crossing of the 4 remaining tendons, a cross-hair is added at the rear of the instrument.

II. CONCEPT

This section elaborates on conceptual decisions in the design of the experimental setup. Figure 2 shows an overview of the setup design. Various components and details of this setup will be discussed.

A. *Ultrasound*

Ultrasound images are obtained by a Siemens Acuson S2000$^{\text{TM}}$(Siemens AG, Erlangen, Germany) ultrasound machine. The 2D probe (18L6 HD) is positioned above the tip of the instrument, where the instrument tip should touch the ultrasound image plane, see figure 3. When bent, the instrument tip moves out of the ultrasound plane.

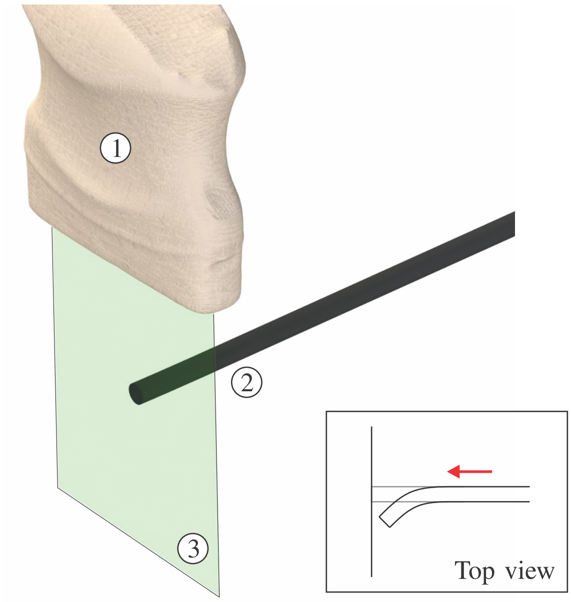

Fig. 3. 2D ultrasound image is captured by the ultrasound probe ① of the tip of the instrument. The instrument tip ② moves out of the ultrasound plane ③ if it is bent; this out-of-plane movement is compensated by moving the instrument forwards.

In order to keep the instrument tip in the ultrasound plane, the out-of-plane motion needs to be compensated. It is chosen to move the instrument assembly rather than the ultrasound probe, because of future work. A completely integrated system should compensate for three degrees of freedom, and allowing the instrument assembly to move forwards and backwards enables this. Water is chosen as the ultrasound medium, which also means a water tank is needed. The ultrasound probe is suspended with the transducer surface just below the water level.

B. *Actuation*

Many continuum robot actuation systems in literature [2]–[5] have a separate motor per tendon. The DEAM instrument has antagonistic tendons, i.e. it uses two tendons per degree

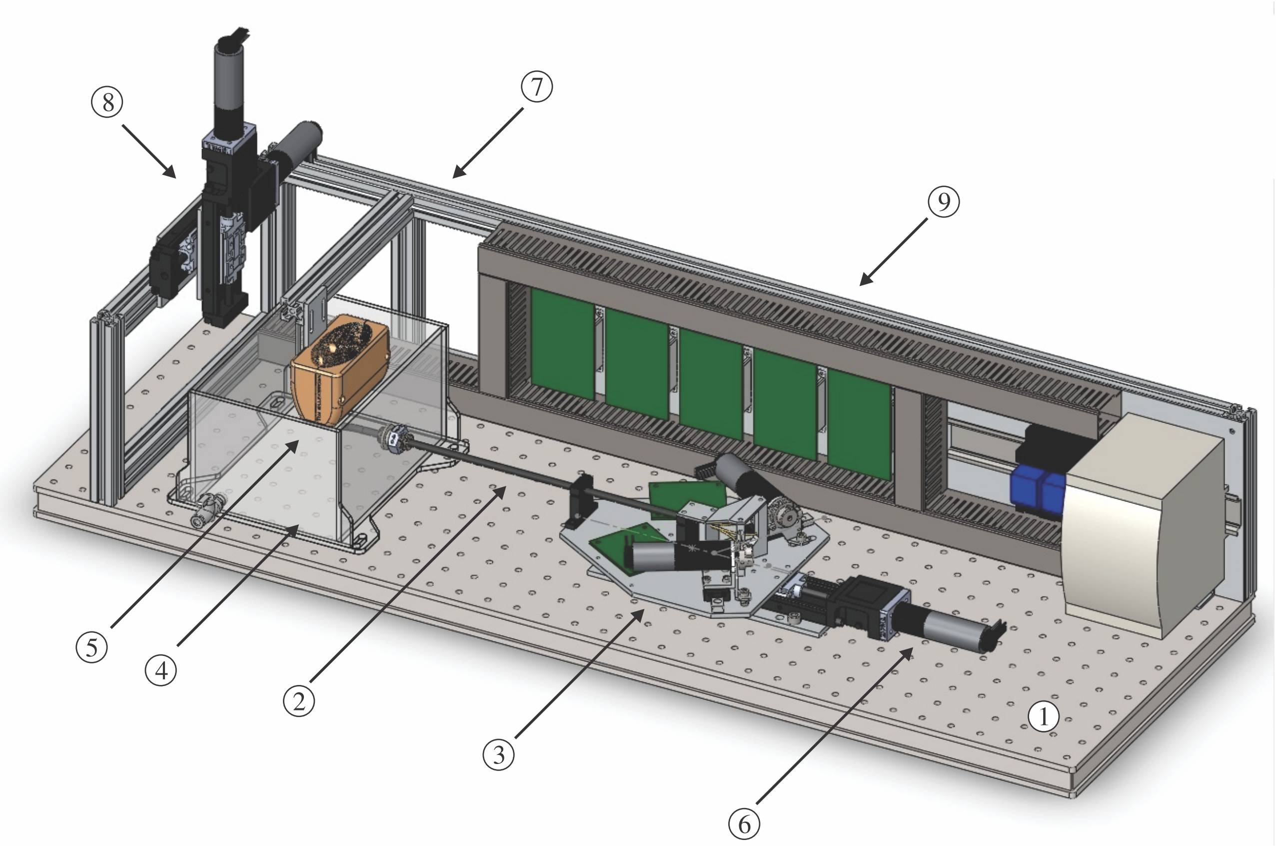

Fig. 2. Overview of the setup, mounted on an optical breadboard ①. The instrument ② is mounted to the instrument assembly ③ and enters the water tank ④ trough an interface. The ultrasound probe can be mounted in the probe clamp ⑤. The instrument assembly can be moved forwards and backwards by the instrument linear stage (z stage) ⑥. An aluminium frame ⑦ holds the environment simulator ⑧ and electrics ⑨.

of freedom. It is opted to use one motor per degree of freedom to explore the possibilities of using such a drive system. In terms of cost and space, for a commercial application, this option is preferred. Note that this decision does impose additional control difficulties.

C. Environment simulator

The setup is equipped with 'environmental motion', i.e. linear stages are mounted that can mimic environment (simulated heart) motion in 2D. The environment stages are placed and functional, but are not used in this project.

D. Orientation

The instrument tip should be in the water and it is chosen to keep the tendons dry. For both simplicity and future work, it has been chosen to keep the assembly horizontal and thus a watertight interface between tank and instrument is needed. This interface is a grease-filled o-ring port, as depicted in figure 4.

E. Tendon routing

Tendon routing is needed to minimize friction and to ensure reliable operation. For serviceability reasons the motors and pulleys should be easily reachable and the number of moving (rotating) parts should be minimal. It is decided that the tendons are routed using the Bowden-cable concept, where the tendon sleeves are made of brass. See figure 5 for its construction. Brass material is self-lubricating and has low friction by nature, which can be further reduced by filling the sleeves with oil or grease. The Bowden-cable concept allows freedom in motor placement, the motors are placed such that they can easily be serviced. The concept is chosen over concepts with cable pulleys and no tendon-guidance.

F. Pretension

Pretension should be put on the tendons, in order to prevent backlash in the Bowden guides. Pretension allows an immediate response of the instrument tip to a movement of its actuator. The pretension mechanism is shown in figure 6. This concept, which rigidly fixes the motor assembly to the base plate, is preferred over concepts applying pretension by springs. With springs as pretension mechanism, a mass-spring system is created, of which the resonance frequency should be higher than the resonance frequency of the tendon/tip system. Given the weights of the components, this is not trivial and springs were considered too risky. Hence, the rigid pretension mechanism was chosen.

III. REQUIREMENTS

To minimize development time of the setup there should be as much re-use of existing work as possible. The decided prerequisites are:

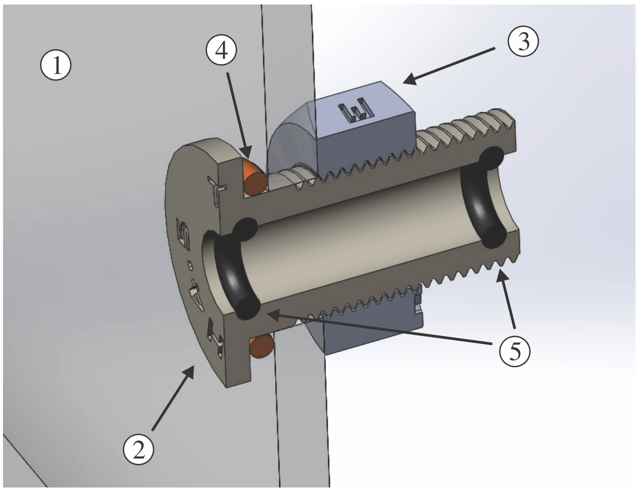

Fig. 4. The interface between water tank ① and instrument. Interface body ② is tightened using nut ③, an o-ring ④ seals the body to the tank. Greased o-rings ⑤ stop water pouring out of the port, while allowing linear movement of the instrument.

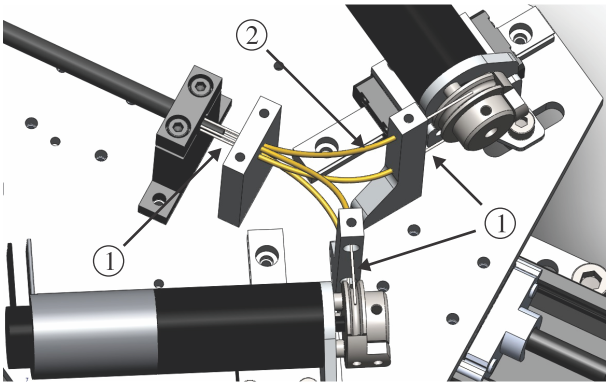

Fig. 5. Bowden cable construction. The tendons ① are routed from the instrument to the motors via brass Bowden guides ②. The motors are placed such that they can be easily reached.

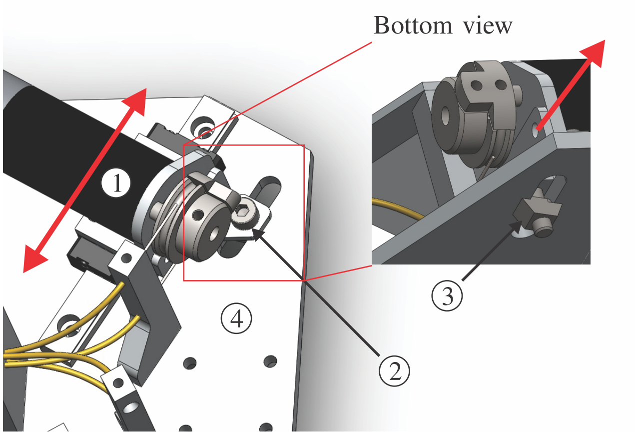

Fig. 6. Pretension mechanism. The motor assembly ① is mounted to a linear slide. A force greater than the force required to bend the instrument tip should be applied to the motor assembly, placing tension on the tendons (see insert). Tension remains in the tendons when tightening bolt ②; Nut ③ secures the motor assembly to the instrument base plate ④.

- Maxon brushless DC motors (Maxon Motor AG, Sachseln, Switzerland) are used for all actuation.
- Elmo Whistle 2.5/60 motor controllers (Elmo Motion Control Ltd., Petach-Tikva, Israel) are used connected to a CAN network.
- Control software will run on a Windows 7 desktop computer.
- The software should use the same framework as the needle steering setup of the RaM group [RaM, University of Twente, Enschede, The Netherlands].

IV. MECHANICAL DESIGN

This section explains the mechanical design considerations.

A. *Linear motor motion*

According to [6], the mitral valve of the human heart reaches a maximum velocity of 210 mm/s and an acceleration of 2800 mm/s^2. These figures are used as requirements for all actuation in PLATINUM. For linear stages, situation of figure 7 applies. The limiting motor is the Environment Horizontal stage because it is moving the greatest mass.

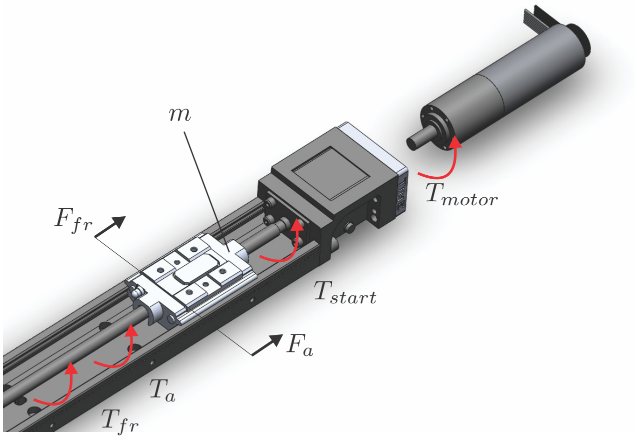

Fig. 7. Situation for calculating the required torque on the linear stage motors. T_{motor} is the total torque experienced by the motor gearbox, T_{start} is the starting torque determined by the linear stage, T_{fr} is the result of friction and T_a is the torque resulting of mass acceleration.

Total motor torque is:

$$T_{motor} = T_{start} + T_{Fr} + T_a \tag{1}$$

Where T_{start} is determined by the linear stage, $T_{fr} = F_{fr} \cdot d_l$ is the friction torque and $T_a = m \cdot a_{min} \cdot d_l$ is the result of accelerating the mass. In the above d_l is the lead of the linear stage, m is the accelerated mass and a the required acceleration. For $T_{start} = 1.2$ Ncm, an estimated $F_{fr} = 0,5$ N, $m = 0,8$ kg, $d_l = 5$ mm and $a_{min} = 2800$ mm/s^2 the required motor torque is $0,0279$ Nm. A Maxon Motor combination EC-max 22 25W, GP22HP gearbox and Type M Encoder MR with 128 ticks per revolution are selected.

B. Instrument motor motion

The minimal velocity mentioned by Kettler et al. is used to calculate the requirements on the motors driving the tendons (instrument motors) [6]. Because the instrument tip has a low mass, the acceleration is assumed to be sufficient. The situation of figure 8 applies.

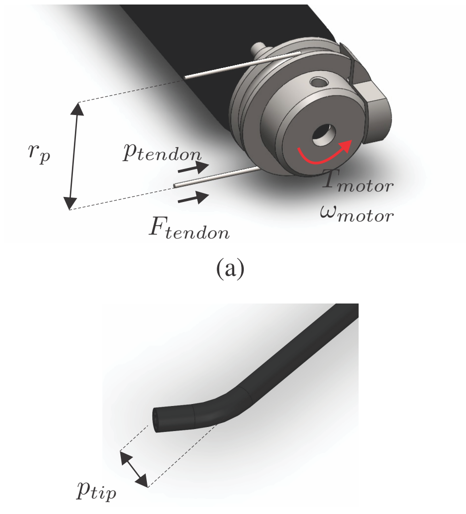

(a)

(b)

Fig. 8. Instrument motor torque situation. T_{motor} and ω_{motor} are the torque and rotation velocity of the motor, p_{tip} and p_{tendon} are the positions of respectively the tip and tendon-end and $\dot{p}_{tip}$ is the required velocity.

Total motor torque $T_{motor} = F_{tendon} \cdot r_p$, where F_{tendon} is the tendon force and r_p is the pulley radius. Using $F_{tendon} = 10$ N (measured value for full deflection) and $r_p = 9,315$ mm the required torque is $T_{motor} = 0,095$ Nm.

V. ELECTRICAL DESIGN

Details on the electrical design can be found in Appendix B.

VI. REALIZATION

The system described above is built and a photograph of the realization is given in figure 9.

VII. DELAY

It was found that there is a time delay present in the system. The delay of interest occurs between movement of the instrument tip and measurement signals arriving at the controller. The total delay is found to be 0.8 seconds. This number is found from multiple measurements at different tip velocities. From manual estimations the following breakdown is found:

- $\approx$ 0.3 seconds: Ultrasound machine, estimated by finding the delay between physical movement and reaction on the machine's screen.
- 0.04 seconds: Controller cycle (theoretical value), the controller needs one cycle to respond (or store values).
- 0.04 seconds: Image processing (theoretical value), image processing needs one cycle to compute the device centroid.
- $\approx$ 0.4 seconds: What remains is delay in the image capturing device.

No effort could be made to overcome these delays, but some options are explained in section 'Recommendations'.

VIII. HYSTERESIS

Hysteresis has been identified in the system. Plausible sources for hysteresis in PLATINUM are:

- Backlash in the Bowden cable assembly
- Free play in the motor gearbox
- Free play in the instruments' hinge elements
- Tension causes the tendons to elongate
- Tip 'memory' effect. The shape of the articulated tip is no pure single-section articulation, but the situation of figure 10 is observed.

The individual components are not investigated, because the total hysteresis is likely an addition of the above sources. Hysteresis plots are recorded where the results are manually compensated for the effects of delay. The delay compensated results are given in figures 11 and 12, for the horizontal and vertical axis, respectively.

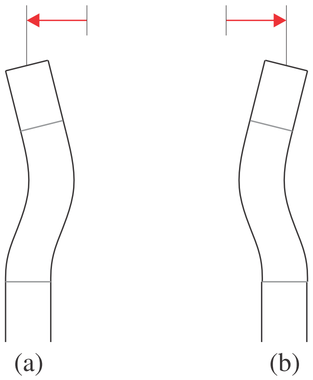

(a) (b)

Fig. 10. (a) Tip top-view when the instrument has moved from the right to the center. (b) Tip top-view when the instrument has moved from the left to the center.

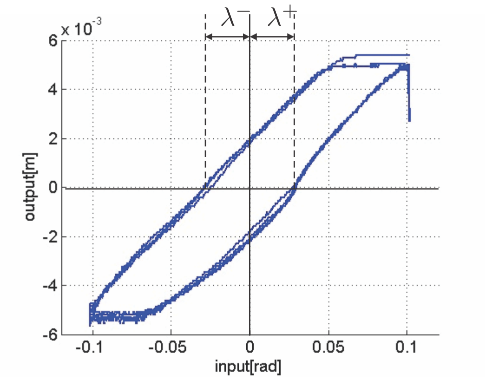

Fig. 11. Hysteresis plot for horizontal DOF. Hysteresis parameters λ^- and λ^+ are indicated, and their sum stands for the hysteresis loop width.

The mechanical hysteresis is determined by calculating the average of all input angles of which the corresponding measurements lie in the window [-2mm,2mm] and distinguish

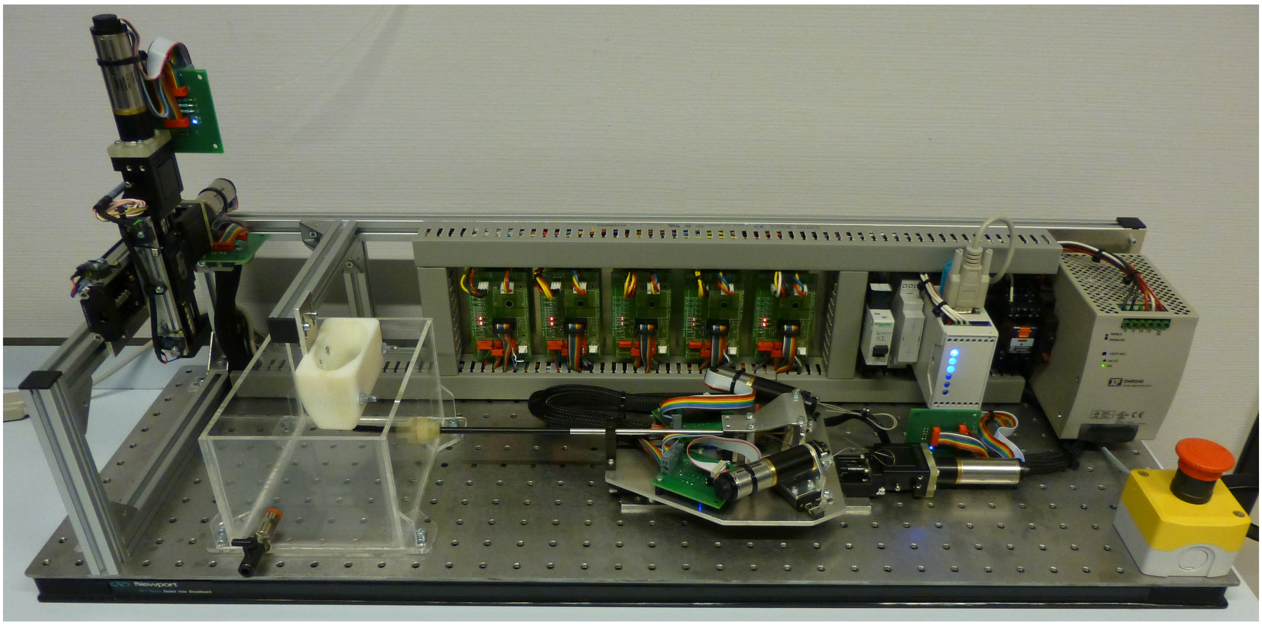

Fig. 9. Photo of the actual setup. All components are mounted to the optical breadboard. The instrument assembly is mounted in the middle, with the instrument piercing the tank. The ultrasound probe mount hangs above the tip in the water tank. Electronics are mounted to the rear-wall of the setup and the environment simulator is mounted at the very left.

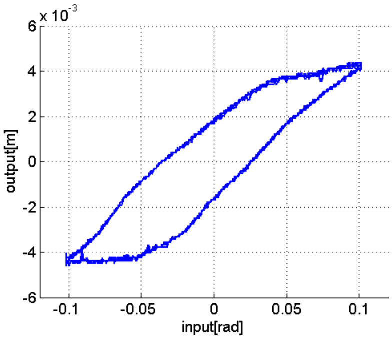

Fig. 12. Hysteresis plot for vertical DOF.

between the upwards and downwards slope. The results are depicted in table I.

DOF	λ^- [rad]	λ^+ [rad]
Horizontal	-0,029	0,025
Vertical	-0,031	0,024

TABLE I

MEASUREMENT OF MECHANICAL HYSTERESIS.

REFERENCES

[1] P. Breedveld, "Kinematics for multisection continuum robots," in *Proceedings of the Design of Medical Devices Conference*, 2010.

[2] M. W. Hannan and I. D. Walker, "Kinematics for multisection continuum robots," *IEEE Transactions on Robotics*, vol. 20, no. 2, pp. 45–63, 2003.

[3] B. A. Jones and I. D. Walker, "Kinematics for multisection continuum robots," *IEEE Transactions on Robotics*, vol. 22, no. 1, pp. 43–55, 2006.

[4] D. B. Camarillo, C. F. Milne, C. R. Carlson, M. R. Zinn, and J. K. Salisbury, "Mechanics modeling of tendon-driven continuum manipulators," *IEEE Transactions on Robotics*, vol. 24, pp. 1262–1273, 2008.

[5] M. W. Hannan and I. D. Walker, "A modeling approach for continuum robotic manipulators; effects of nonlinear internal device friction," *IEEE/RSJ International Conference on Intelligent Robots and Systems*, pp. 5139–5146, 2011.

[6] D. Kettler, R. Plowes, P. Novotny, N. V. Vasilyev, P. del Nido, and R. Howe, "An active motion compensation instrument for beating heart mitral valve surgery," in *IEEE/RSJ International Conference on Intelligent Robots and Systems*, pp. 1290–1295, 2007.

Part II

‘Modelling’

Modelling

Tim T.M. Ellenbroek, Gustaaf J. Vrooijink, Roy J. Roesthuis and Sarthak Misra
University of Twente, The Netherlands

***Abstract*— This article will explain the steps taken to realize a model for the robotic instrument. The modelling of continuum robots is introduced in section I. The specific and independant transforms are explained in sections II and III. The complete forward model is given in section IV and the inverse model is given in section V. Section VI explains the use of the models in control.**

I. INTRODUCTION

Continuum robots are often modelled using a constant curvature approach [1], this research follows in adopting this modelling approach. Figure 1 shows a simplified shape of an articulated continuum instrument.

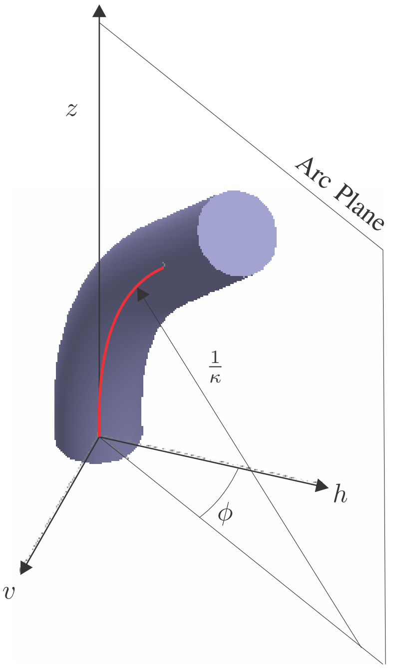

Fig. 1. Continuum robot. Arc plane angle ϕ and robot curvature κ model the shape of the robot. The length of the articulating part of the robot (indicated in red) is l_a.

The instrument under development uses 4 tendons to operate 2 degrees of freedom (DOF). The instrument is mounted horizontally as indicated in figure 2, such that one tendon-pair bends the instrument in horizontal direction, a second tendon-pair bends the instrument in vertical direction. The directions are indicated with respectively subscripts $_h$ and $_v$.

Applying the model description of [1] to the robotic instrument under development results in figure 3.

The inputs of the model are the two motor angles θ_h and θ_v, the output of the model is tip position $\mathbf{p}$. The shape

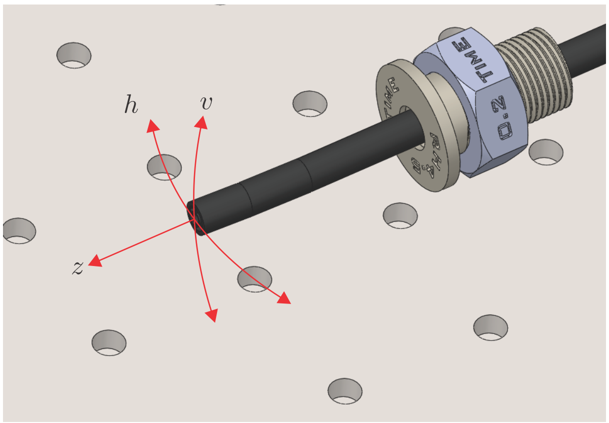

Fig. 2. Instrument mounting orientation. One tendon-pair bends the instrument in horizontal direction, a second tendon-pair bends the instrument in vertical direction.

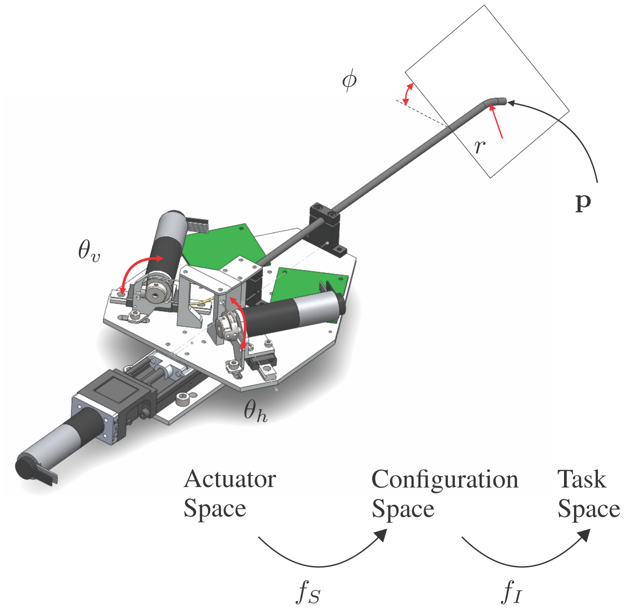

Fig. 3. Space and Transformation model. The Actuator space is given by the two motor angles θ_h and θ_v. Arc curvature $\kappa = \frac{1}{r}$ and arc plane angle ϕ make up the Configuration space and instrument tip position $\mathbf{p}$ is the Task space. Specific transform f_S and independent transform f_I convert between the spaces as indicated.

of the articulated tip is determined by curvature κ and arc plane angle ϕ and are calculated by $(\phi, \kappa) = f_S(\theta_h, \theta_v)$. Independent transform $\mathbf{p} = f_I(\phi, \kappa)$ is found in [1].

The following sections will explain the use of the specific transform, the independent transform, describe the inverse transform, identify hysteresis and will discuss the usage of the transforms in control.

II. Specific Transformation

The motor angles θ_h and θ_v are translated to linear tendon shortening, as figure 4 indicates, using:

$$\begin{aligned} \delta_h &= r_p \cdot \theta_h \\ \delta_v &= r_p \cdot \theta_v \end{aligned} \tag{1}$$

Where r_p is the radius of the motor pulley.

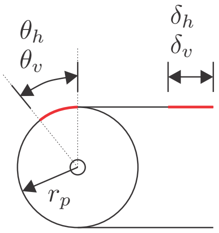

Fig. 4. Rotary to translation motion at motor pulley. θ_h (or θ_v) causes a movement (δ_h or δ_v) of the tendon on the pulley, indicated in red. The red displacements are equal in length and, given constant pulley radius r_p, have a linear relation to motor angle.

A rotary motion of the motor winds the tendon around the pulley by δ_h (or δ_v), which is equal to the tendon shortening experienced by the instrument. δ_h and δ_v are converted to configuration parameters using the transform that is derived using figure 5.

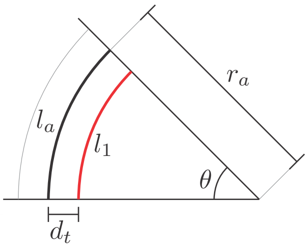

Fig. 5. 2D view of a bent instrument. The backbone (bold line) has length l_a and tendon 1 (red), at distance d_t from the backbone, has length $l_1 = l_a - \delta_1$, where δ_1 is the shortening of tendon 1. Situation $l_1 < l_a$ causes the instrument to bend with radius r_a.

The bent instrument is modelled by a planar arc. $l_1 = l_a - \delta_1$ with $\delta_1 > 0$ makes the instrument bend with curvature κ_1. Given $\kappa_1 = \frac{1}{r_a}$ the following holds:

$$\theta = \frac{l_a}{r_a} = \frac{l_a - \delta_1}{r_a - d_t}$$

where l_a, d_t are defined in figure 5. Solving for r_a yields:

$$\kappa_1 = \frac{1}{r_a} = \frac{\delta_1}{l_a \cdot d_t} \tag{2}$$

Similarly, $\kappa_2(\delta_2)$ can be found.

Now, let $\kappa_h = \kappa_1$ and $\kappa_v = \kappa_2$. Assuming a symmetrical instrument, from Hannan et al. we find that two orthogonal sets of curvatures produce an effective curvature by $\kappa = \sqrt{\kappa_h^2 + \kappa_v^2}$ [2]. The plane angle $\phi = \arctan\left(\frac{\kappa_v}{\kappa_h}\right)$. Thus, inserting (1) we find the magnitude and angle of the bent instrument:

$$\kappa = \frac{r_p}{l_a \cdot d_t} \sqrt{\theta_h^2 + \theta_v^2} \tag{3}$$

$$\phi = \arctan\left(\frac{\theta_v}{\theta_h}\right) \tag{4}$$

In the above θ_h and θ_v are the motor angles that operate the respectively horizontal and vertical tendon pair.

III. Independent Transformation

Please consider figure 6. Given κ, ϕ and an intermediate frame Ψ_1, f_I maps any coordinate of Ψ_1 to the global frame Ψ_0. The instrument under development has a straight section l_t, starting at the origin of Ψ_1 and defining the origin of Ψ_t. Point p is defined as the origin of Ψ_t.

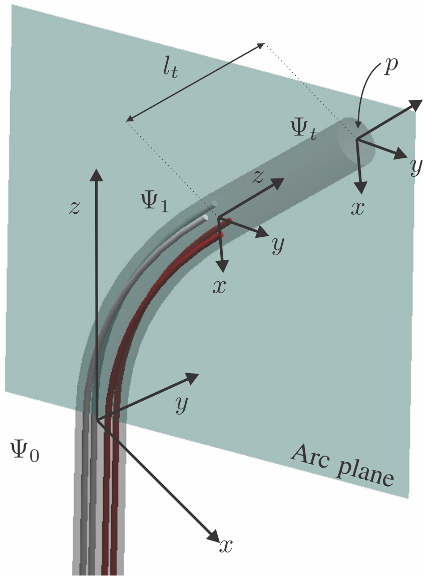

Fig. 6. Functional view of the bent section of the instrument. The tendons coloured red are pulled, causing the instrument to bend. Global frame Ψ_0, intermediate frame Ψ_1 and tip frame Ψ_t, at distance l_t from Ψ_1, are indicated, with their respective direction definitions. Point p is defined as the origin of Ψ_t.

Webster et al. present a transformation that converts any coordinate in Ψ_1 to a coordinate in Ψ_0 [1]. Point p is modelled as a vector ${}_1\mathbf{p}$, where the subscript indicates that point p is expressed in frame Ψ_1. Using ${}_1\mathbf{p} = \begin{bmatrix} 0 & 0 & l_t \end{bmatrix}^T$ reduces Webster's approach to:

$${}_0\mathbf{p} = \begin{bmatrix} \cos(\phi)\left\{\frac{1}{\kappa}(1 - \cos(\kappa l_a)) + l_t \sin(\kappa l_a)\right\} \\ \sin(\phi)\left\{\frac{1}{\kappa}(1 - \cos(\kappa l_a)) + l_t \sin(\kappa l_a)\right\} \\ \frac{1}{\kappa}\sin(\kappa l_a) + l_t \cos(\kappa l_a) \end{bmatrix} \tag{5}$$

IV. FORWARD TRANSFORMATION

The complete forward kinematics are given by:

$$\mathbf{p} = f_I\left(f_S\left(\theta_h, \theta_v\right)\right) \tag{6}$$

In other words, the tip position is found via (5), using κ and ϕ from respectively (3) and (4).

V. INVERSE TRANSFORMATION

The input of the inverse model is a processed 2D ultrasound image. This gives $\bar{\mathbf{p}} = \begin{bmatrix}\bar{x} & \bar{y}\end{bmatrix}^T$, where the bar indicates a measurement. No analytical solution for κ as function of $\bar{\mathbf{p}}$ can be found, hence a numerical approximation is used. Figure 7 shows the ultrasound image plane and the approximated curvature.

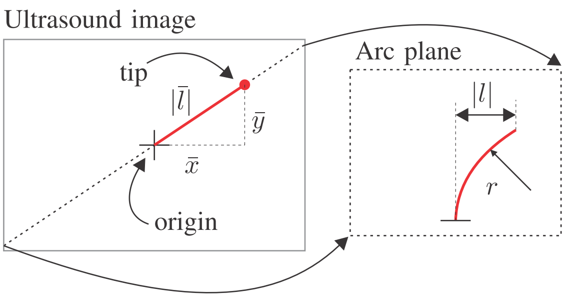

Fig. 7. Measurements from the ultrasound image. The curvature of the instrument r^{-1} is approximated using distance $|l|$ from the origin to the tip position.

The inverse model algorithm is shown in Algorithm 1. $\bar{\phi}$ is calculated from $\bar{\mathbf{p}}$, $\hat{\theta}_h$ and $\hat{\theta}_v$ are calculated by the algorithm, where the hat indicates an estimate or approximation. The iterative approach starts with a rough estimate of κ and uses a proportional-integral update (with gain G) of approximation variable κ_k. The algorithm stops if approximated l_k is close enough to measured $|\bar{l}|$. Estimate l_k is calculated from κ_k using f_I', where f_I' is a simplified version of f_I that merely calculates l_k.

The iterative loop is guarded by a maximum iteration count and a minimum step size. The maximum iteration count captures the event that $|l_k - |\bar{l}||$ does not converge. The minimum step size captures the event that l_k converges locally, such that $|l_k - |\bar{l}||$ converges to a value other than zero, and can never become smaller than $tolerance$. These guards prevents deadlock in the software.

VI. CONTROL

Babuška presents the Internal Model Control scheme, depicted in Figure 8 [3]. The inverse model transforms the tip position target $\mathbf{r} = \begin{bmatrix}r_x & r_y\end{bmatrix}^T$ to the plant inputs $\hat{\boldsymbol{\theta}}$ and the forward model approximates plant behaviour. $\bar{\mathbf{p}} = \begin{bmatrix}\bar{x} & \bar{y}\end{bmatrix}^T$ and $\hat{\mathbf{p}} = \begin{bmatrix}\hat{x} & \hat{y}\end{bmatrix}^T$ are respectively the actual and simulated tip position and model mismatch $\mathbf{e}$ is fed back to close the loop.

In open-loop measurements only the inverse model and process are used, for closed-loop measurements the forward model is added. For a more complete description of control and control algorithms the reader is referred to the Control description document.

Algorithm 1 Inverse Model Algorithm

```
Require:
    $\bar{x}, \bar{y}$ Measurement

    Approximate:
    calculate $|\bar{l}| = \sqrt{\bar{x}^2 + \bar{y}^2}$
    $\kappa_k = \frac{|\bar{l}|}{l_a + l_t}$                    ▷ Initial estimate
    while $error < tolerance$ do
        calculate $l_k = f_I'(\kappa_k)$
        $error = |l_k - |\bar{l}||$
        $\kappa_{k+1} = \kappa_k + G \cdot error$           ▷ Update estimate
    end while

    Finish:
    calculate $\bar{\phi}(\kappa_k)$
    calculate $\hat{\kappa_x}(\kappa_k, \bar{\phi}), \hat{\kappa_y}(\kappa_k, \bar{\phi})$
    calculate $\hat{\theta_h}(\hat{\kappa_x}), \hat{\theta_v}(\hat{\kappa_y})$
    return $\hat{\theta_h}, \hat{\theta_v}$
```

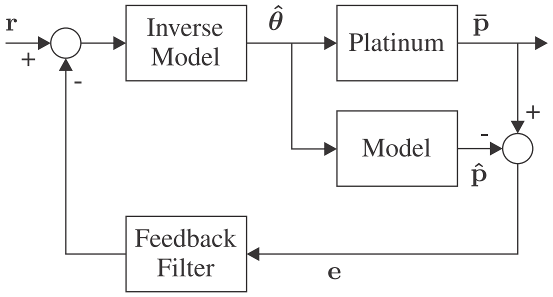

Fig. 8. Internal Model Control scheme. The inverse model is used to control the plant and the forward model is used to compensate for any mismatch between model and plant. $\mathbf{r}$ is a reference signal, $\hat{\boldsymbol{\theta}}$ is the input for the instrument motors, $\bar{\mathbf{p}}$ and $\hat{\mathbf{p}}$ are respectively the actual and simulated tip position and $\mathbf{e}$ is the mismatch between model and actual system.

REFERENCES

[1] R. J. Webster and B. A. Jones, "Design and kinematic modeling of constant curvature continuum robots: A review," *The International Journal of Robotics Research*, vol. 29, no. 13, pp. 1661–1683, 2010.

[2] M. W. Hannan and I. D. Walker, "Kinematics for multisection continuum robots," *IEEE Transactions on Robotics*, vol. 20, no. 2, pp. 45–63, 2003.

[3] R. Babuska, "Knowledge based control systems." Lecture Notes, Delft University of Technology, January 2010.

Part III

‘Control’

Control

Tim T.M. Ellenbroek, Gustaaf J. Vrooijink, Roy J. Roesthuis and Sarthak Misra
University of Twente, The Netherlands

***Abstract*— This article describes the design and implementation of control and software for PLATINUM. Conceptual decisions are discussed in section I, then the method is explained in section II. The controller architecture for Open-loop control (OL), Internal Model Control (IMC) and Extended Kalman Observer (EKO) are explained in sections III, IV and V respectively. A hysteresis compensation technique is explained in section VI.**

I. CONCEPT

There is a model of the behaviour of the instrument available. In control it could be beneficial to use this model in a model-based controller over the use classical PID controllers, because the added knowledge provides estimates. A form of model-based control is the Internal Model Control scheme which is given in figure 1 [1].

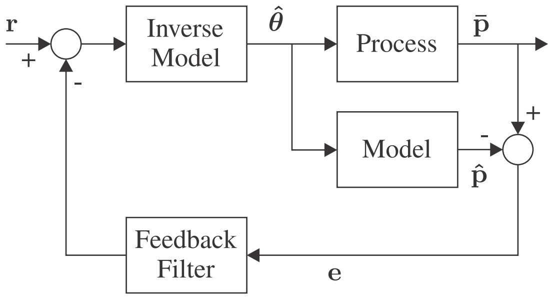

Fig. 1. Internal Model Control scheme. The inverse model is used to control the plant and the forward model is used to compensate for any mismatch between model and plant. $\mathbf{r}$ is a reference signal, $\hat{\boldsymbol{\theta}}$ is the input for the instrument motors. Symbols $\bar{\mathbf{p}}$ and $\hat{\mathbf{p}}$ are respectively the actual and modelled tip position and $\mathbf{e}$ is the mismatch between model and actual system.

The inverse model transforms the desired tip position $\mathbf{r}$ to the plant inputs $\hat{\boldsymbol{\theta}}$ and the forward model approximates plant behaviour. $\bar{\mathbf{p}}$ and $\hat{\mathbf{p}}$ are respectively the actual and simulated tip position. Model mismatch $\mathbf{e}$ is fed back to close the loop. Note that the linear stage of the instrument assembly is controlled in open-loop; i.e. there is no feedback on correct positioning of the stage. Measuring the z position of the tip using 2D ultrasound is difficult, and misalignment of the stage only results in small tip pose measuring errors. Moreover, future use of 3D ultrasound enables measuring the z position of the tip directly.

The control algorithm runs on a PC (Dell Optiplex 980, Intel I7 CPU), and is positioned in the system according to figure 2.

II. METHOD

A. Definitions

The motion directions of the instrument tip are indicated in figure 3. The directions defined here apply to all measurements and experiments.

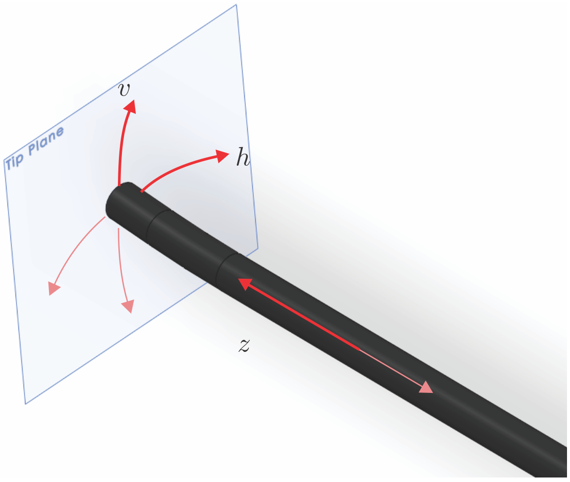

Fig. 3. Instrument tip direction definitions. The positive directions are indicated by bold red lines and DOF indication.

B. Homing procedure

Control assignments and measurements on the motors of PLATINUM are relative to the initial position. For software to obtain an absolute position, a homing procedure is designed. The implemented homing algorithm is outlined in Appendix C.

III. OPEN-LOOP CONTROL

Open-loop control uses the inverse model to calculate the motor angles θ_h and θ_v required to move the tip towards the reference position $\mathbf{r}$, as figure 4 indicates.

Performance of the open-loop controller will be discussed in section 'Experiments'.

IV. INTERNAL MODEL CONTROL

Babuška presented the IMC scheme, depicted in Figure 1 [1]. Applying this scheme to PLATINUM, the situation of figure 5 is obtained.

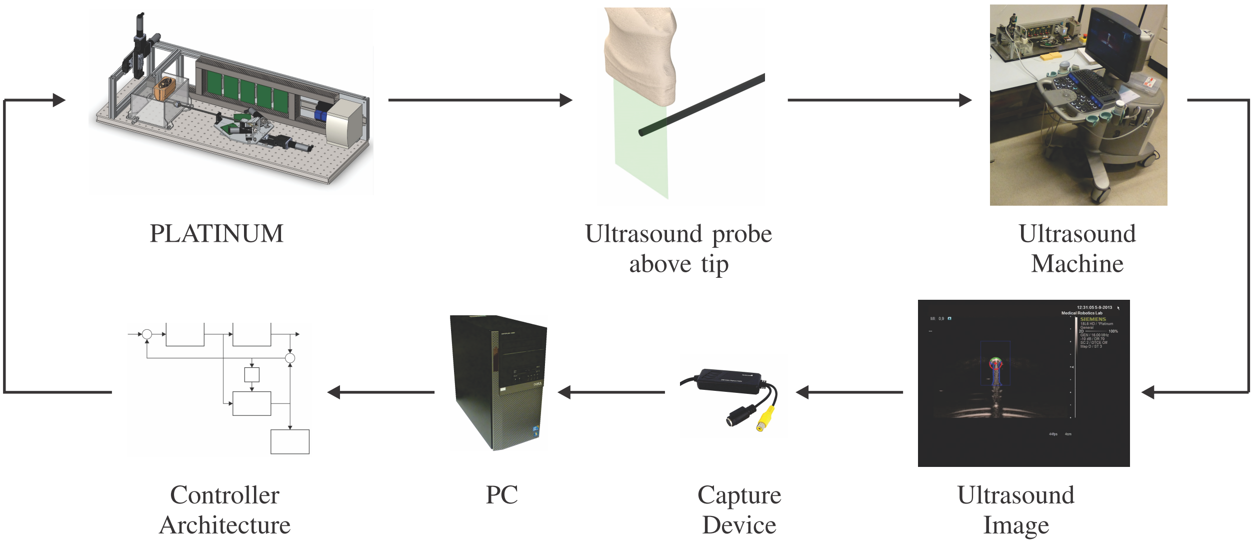

Fig. 2. System loop. PLATINUM receives commands from the controller architecture running on the PC and the tip position is recorded with the ultrasound probe connected to the ultrasound machine (Siemens Acuson S2000, Siemens AG, Erlangen, Germany). The ultrasound images are captured by an s-video capture device and processed by an image processing algorithm on the PC.

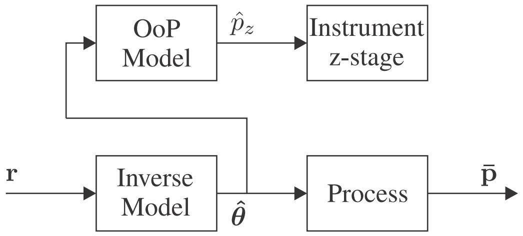

Fig. 4. Diagram of the open-loop controller. Reference $\mathbf{r}$ is fed to the inverse model, which generates control input $\hat{\boldsymbol{\theta}}$ for the process. The Out-of-Plane (OoP) model calculates the out-of-plane movement $\hat{p}_z$ from the reference tip position and drives the instrument linear stage. $\bar{\mathbf{p}}$ is the measured tip position.

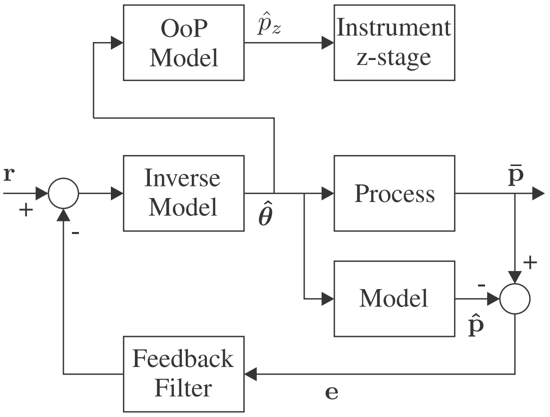

Fig. 5. Internal model control diagram. Most components are equal to the open-loop controller. As before, $\mathbf{r}$ is a reference signal, $\hat{\boldsymbol{\theta}}$ is the input for the instrument motors. Symbols $\bar{\mathbf{p}}$ and $\hat{\mathbf{p}}$ are respectively the actual and modelled tip position and $\mathbf{e}$ is the mismatch between model and actual system.

V. EXTENDED KALMAN OBSERVER

Using ultrasound images for measurements makes likely that measurement noise is not negligible, and the non-ideal behaviour of the instrument (mismatch from model) can be modelled as process noise. Moreover, image processing may not always be able to detect the instrument tip. For these situations the Kalman Observer could be a possible improvement over IMC, since the Kalman Observer is able to model process and measurement noise and calculate its state estimate on both model and (previous) measurements. The above considerations make the Kalman Observer theoretically suited for use with PLATINUM. Because the model of the instrument is non-linear, the Extended Kalman Observer (EKO) is used. The EKO control diagram is given in figure 6.

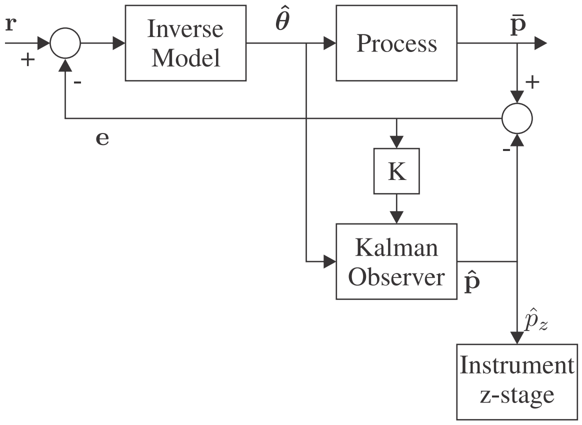

Fig. 6. Kalman Observer in the control loop. State estimation $\hat{\mathbf{p}}$ is the estimated tip position. The feedback signal is the mismatch between $\bar{\mathbf{p}}$ and $\hat{\mathbf{p}}$. The z stage is controlled using $\hat{p}_z \in \hat{\mathbf{p}}$. No OoP model is required.

Note that due to the absence of dynamics in the model some of the equations in the EKO reduce to static equations, and hence predicting performance is affected.

A. *Verification*

The IMC is compared to the EKO. The motion profile for these measurements is a circle with a radius of 6mm and a tip velocity of 2.4mm/s. The controller frequency equals the ultrasound capture frequency of 25Hz. Figures 7 and 8 show the results of these measurements, where the initial offset (due to hysteresis) is manually compensated.

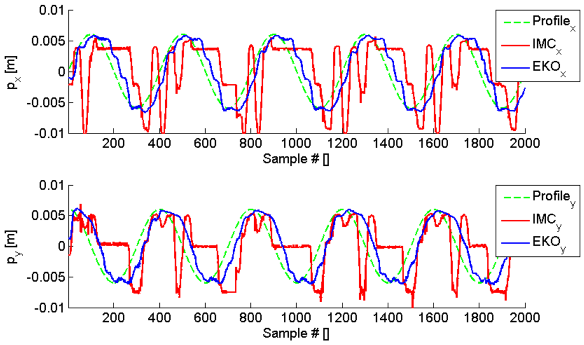

Fig. 7. Comparison of IMC and EKO performance. The upper graph shows the x tip position and the lower graph shows the y position. IMC responds aggressive to process/model mismatches, EKO response is cleaner.

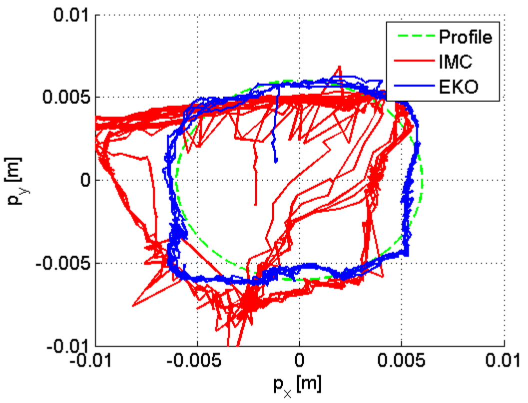

Fig. 8. Comparison of IMC and EKO performance. Five cycles are shown for both controllers. EKO response is cleaner than IMC, and EKO shape is closer to profile than IMC.

Table I summarizes the RMS errors of each cycle for both the IMC and EKO controllers. It can be seen that the tracking performance increases for the EKO. RMS errors decrease from 5.22mm to 1.88mm and from 2.84mm to 2.45mm, for the x-direction and y-direction, respectively.

The EKO controller is more able to maintain the target profile, so its RMS errors are lower than those of the IMC controller.

Based on these results, no further measurements are performed using IMC. Comparisons will be made between open-loop and EKO systems.

	RMS errors			
	IMC_x [mm]	IMC_y [mm]	EKO_x [mm]	EKO_y [mm]
Cycle 1	5.59	4.64	1.85	2.57
Cycle 2	5.13	5.53	1.87	2.38
Cycle 3	5.02	3.95	1.85	2.41
Cycle 4	5.42	4.98	1.88	2.44
Cycle 5	4.94	5.11	1.97	2.44
Mean	5.22	4.84	1.88	2.45
σ	0.25	0.53	0.05	0.06

TABLE I

IMC VS EKO PERFORMANCE

VI. HYSTERESIS COMPENSATION

Hysteresis was identified in section 'Platinum'. To improve response time of the tip to actuator movement hysteresis compensation is applied. Figure 9 shows the location of hysteresis compensation in the control loop.

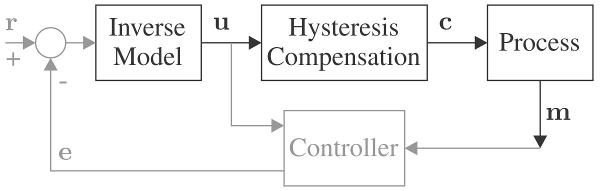

Fig. 9. Hysteresis compensation in control loop. Input of the compensator is $\mathbf{u}$, the output of the compensator is $\mathbf{c}$ and the measurement is defined $\mathbf{m}$. Note that $\mathbf{c}$ is only fed to the actual process (not to the model).

Reilink et al. present a hysteresis reduction technique for the class of robotic continuum style medical equipment [2]. The proposed hysteresis reduction technique is aimed at reducing fast actuator behaviour if the surgeon's hand oscillates slightly. Given the similar clinical environment, the technique is applicable to our system. Reilink applies a hysteresis model with essentially two modes: contact and free. Contact mode is detected by a criterion that checks if the difference between the actuator input derivative Δc and the measured output derivative Δm is below a certain threshold, i.e. contact is detected if $|\Delta c - \Delta m| < threshold$. However, with PLATINUM, the hysteresis loop observed is not always symmetrical, as can be seen in figure 10. In that case the time that $|\Delta c - \Delta m|$ is below the threshold differs between the positive and negative direction. This causes the actuator signal c to drift.

Because of the observed drift in algorithms like Reilink's, a classical hysteresis compensator is constructed. The outline is shown in algorithm 1. It detects a sign change in the input, and applies a step in actuator value equal to the mechanical hysteresis $(\lambda^+ - \lambda^-)$.

The compensator prevents drift by prohibiting sequential compensation actions for the same slope, i.e. only one action per slope is allowed. To prevent unnecessary fast actuator behaviour around $\Delta u = 0$ (i.e. the input is almost constant) the condition $|\Delta u'| > threshold$ is used, that requires the input has moved a certain distance from the last sign change before hysteresis is applied.

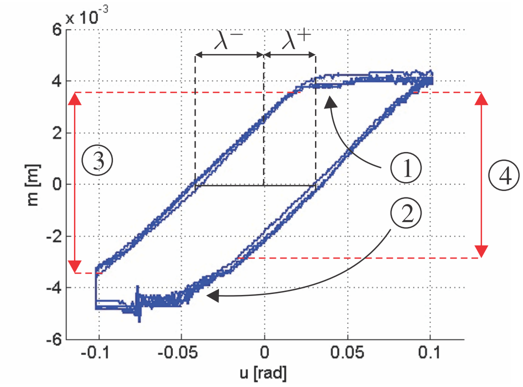

Fig. 10. Non-symmetrical hysteresis plot. The corner top-left ① is sharper than the corner bottom-right ②. This makes criterion $|\Delta c - \Delta m| < threshold$ true for longer on the downwards slope ③ than on the upwards slope ④. The hysteresis parameters λ^- and λ^+ are also defined.

Algorithm 1 Hysteresis compensation

```
Require:
    $\Delta u'$ = change in $u$ since last sign-change detection
    $\Delta u_k$ = change in $u$ since last step
    Detect:
    if $sign(\Delta u_k) \neq sign(\Delta u_{k-1})$ & $|\Delta u'| > threshold$ then
        $\rho = sign(\Delta u') \cdot (\lambda^+ - \lambda^-)$
    else
        $\rho = 0$
    end if
    Compensate:
    $c_k = c_{k-1} + \Delta u_k + \rho$
```

A. Verification

The hysteresis compensator is function tested. Since delay was found present in the system, the tip velocity is kept low and the target profile given in figure 11 is used. The tip is held at the extreme positions for a certain time to ensure delay does not affect hysteresis loop shape. Note that delay may still affect the width of the hysteresis loop.

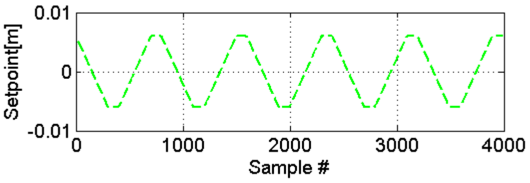

Fig. 11. Target profile for hysteresis compensation verification.

The measurements are performed using a controller frequency of 2.5Hz, which is the same for all evaluation measurements. The reader is referred to section 'Experiments' for more information about the settings with which measurements are performed. The tip velocity is lower than those of the evaluation measurements -to minimize the effects of delay- and equals 1mm/s.

Figure 12 shows the compensation algorithm's activity. If a sign change in Δu is detected (if u changes direction) the compensation action is performed. Since only one sequential compensation action per direction is allowed, this algorithm is drift-free even in the case of a non-symmetrical hysteresis plot.

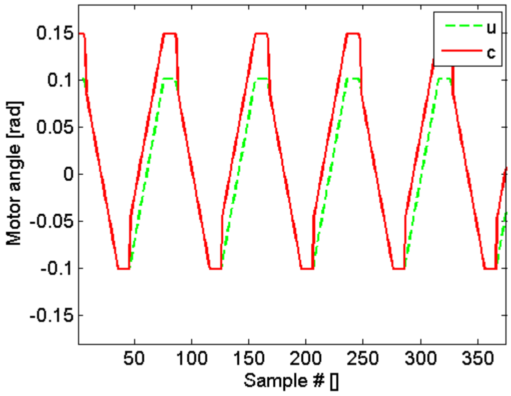

Fig. 12. Input signal u and actuator input c using hysteresis compensation, horizontal DOF. An identical plot is obtained for the vertical DOF. At a direction change of u (sign change of Δu) the compensation action is visible and c steps by the amount $(\lambda^+ + \lambda^-)$.

Figures 13 and 14 show the hysteresis plots for the horizontal and vertical DOF, respectively. For these measurements the estimated parameters $\lambda^+ = 0.0241$ [rad] and $\lambda^- = -0.02353$ [rad] are used, for both axis.

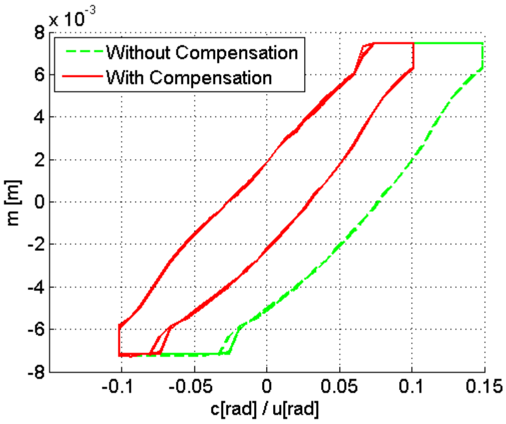

Fig. 13. Hysteresis plot for horizontal DOF.

Values for λ^- and λ^+ are obtained the same way as the identification of hysteresis in the setup, please see section 'Platinum' for more information. Table II shows the results of the hysteresis compensation.

	Without Compensation	With Compensation
	$\lambda^+ - \lambda^-$[rad]	$\lambda^+ - \lambda^-$[rad]
Horizontal	0.1006	0.0530
Vertical	0.0973	0.0497

TABLE II

HYSTERESIS COMPENSATION RESULTS

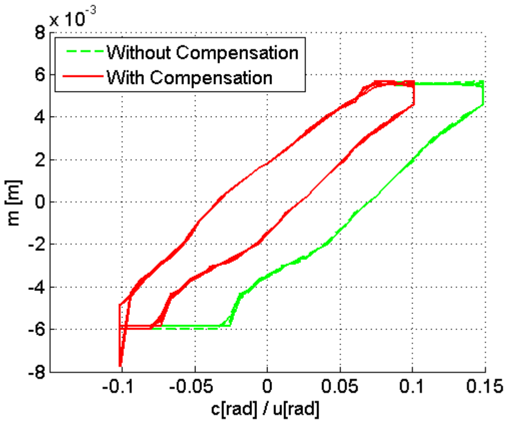

Fig. 14. Hysteresis plot for vertical DOF.

The results show that the hysteresis is reduced by 52.68% and 51.08% for the horizontal and vertical axis, respectively. However, the algorithm is designed to compensate the entire hysteresis. The differences between uncompensated and compensated numbers are equal to the parameter $\lambda^+ - \lambda^-$[rad], proving correct compensation functionality. Some possible causes for this effect exist:

- Under-estimation of hysteresis parameters. The width of the measured hysteresis loop is wider than that of earlier measurements and wider than the mechanical hysteresis loop.
- Delay influences the hysteresis width. Increased delay results in a wider loop, since the measurement lags behind the input. A (constant) delay may also cause a velocity dependant hysteresis loop width.

Section 'Recommendations' will provide ideas and guidance for improving hysteresis compensation performance.

REFERENCES

[1] R. Babuska, "Knowledge based control systems." Lecture Notes, Delft University of Technology, January 2010.

[2] R. Reilink, S. Stramigioli, and S. Misra, "Image-based hysteresis reduction for the control of flexible endoscopic instruments," *Mechatronics*, vol. 23, no. 6, p. 652658, 2013.

Part IV

‘Experiments’

Experiments

Tim T.M. Ellenbroek, Gustaaf J. Vrooijink, Roy J. Roesthuis and Sarthak Misra
University of Twente, The Netherlands

***Abstract*— This section presents the results of the trajectory tracking experiments performed with PLATINUM. The settings used for the experiments are explained, section III shows results of Open-loop (OL) control and Extended Kalman Observer (EKO) control and section IV show results of OL and EKO control combined with Hysteresis Compensation (HC).**

I. CONTROLLER PARAMETERS

PLATINUM has a number of parameters, this section explains how certain parameter values are found.

A. Controller frequency

The experiments in this section focus on being able to compensate for motions of the heart caused by respiration. The shape of this motion is a triangle wave, its peak-to-peak amplitude is found 5.0mm and its frequency is found to be $f_r = \frac{1}{3}$ Hz [1] [2]. Similar results are found in [3]. Because motion is a triangle wave we estimate the need to track a multiple of the fundamental frequency, so the measuring frequency should be about 1Hz. To be able to reconstruct the signal from the measurement, about 4 points per period are required, which makes measurement frequency $f_m = 4$ Hz. It is expected that the delay in PLATINUM and its hardware and software can be brought down to about 0.3 seconds, equalling the delay of the ultrasound machine itself. Possibilities realize this reduction of delay are explained in section 'Recommendations'. Assuming $f_m = 4$ Hz and 0.3 s delay, we theoretically have $0.3 \cdot 4 = 1.2$ frames delay, which means that measurement lags 2 frames. In the current system, to have 2 frames delay (using the current delay estimate of 0.8 seconds) we need the controller frequency to be:

$$f'_{CTRL} = \frac{2}{0.8} = 2.5[Hz] \tag{1}$$

Where prime indicates a scaled value.

B. Tip velocity

Assuming $f_r = \frac{1}{3}$ Hz the motion is modelling as a sine wave $r = A \cdot \sin(2\pi \cdot f_r \cdot t)$. Modelling the motion as a sine wave will result in a slightly higher velocity, hence the actual required velocity will be smaller making the calculated velocity a safe estimate. Given r, the velocity will be $\dot{r} = A \cdot 2\pi \cdot f_r \cdot \sin(2\pi \cdot f_r \cdot t)$. The maximum velocity, using $A = 2.5$ mm, is:

$$\dot{r}_{max} = 2\pi A f_r = 5.24mm/s \tag{2}$$

Because the controller frequency is tuned down to simulate a situation with reduced delay, velocity $\dot{r}_{max}$ should also be scaled relative to the controller frequency. Using expected 0.3 seconds delay and actual 0.8 seconds delay we find:

$$\dot{r}'_{max} = 1.96mm/s \tag{3}$$

The calculated $\dot{r}'_{max}$ will be used in measurements evaluation controllers.

II. METHOD

Controllers are evaluated using three target profile shapes:

- Circle
- Square
- Figure 8

For all experiments in this section, the offset due to hysteresis is manually removed. This offset is a result of hysteresis and dependent on previous movement of actuators and position of the tip. Removing the offset enables us to fairly compare results.

Results will be presented by showing the tip position in an XY plot (the ultrasound image plane) and by plotting the tip's horizontal (x) and vertical (y) positions versus time (sample #). The RMS errors with respect to the target profile are given.

III. CONTROLLER EVALUATION

The differences between Open-loop (OL) control and Extended Kalman Observer (EKO) control were investigated. These results indicate the performance gain of EKO over OL. Each target profile is treated separately.

A. Circle

Figure 1 shows the plot of the tip position in the ultrasound image plane. Figure 2 shows the X and Y positions individually. Table I shows the RMS errors of the measurement for this target profile.

	RMS errors			
	OL x[mm]	OL y[mm]	EKO x[mm]	EKO y[mm]
Cycle 1	3.01	3.78	1.86	2.46
Cycle 2	3.39	3.71	1.89	2.21
Cycle 3	3.39	3.71	1.90	2.22
Cycle 4	3.39	3.71	1.92	2.24
Cycle 5	3.39	3.73	1.92	2.25
Mean	3.31	3.73	1.90	2.28
σ	0.15	0.03	0.02	0.09

TABLE I
CONTROLLER EVALUATION: CIRCLE. THE EKO IMPROVES PERFORMANCE OF OL BY 43% AND 39% FOR x AND y, RESPECTIVELY.

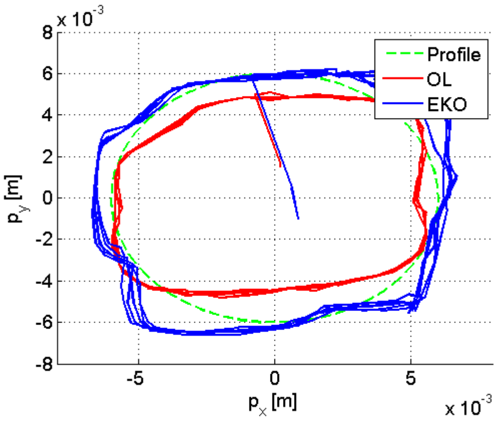

Fig. 1. XY plot of the tip position in the ultrasound image plane. Five cycles are shown for both controllers. Compared to OL, the EKO better matches the target profile's amplitude.

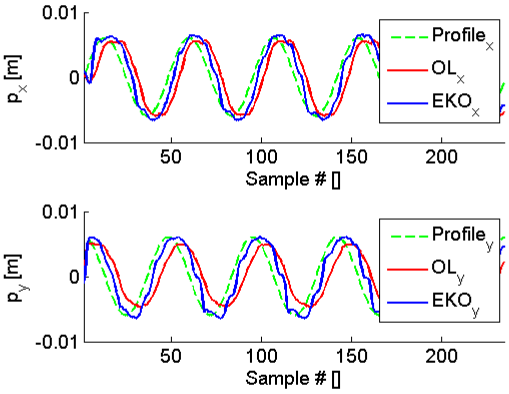

Fig. 2. Horizontal and vertical positions of the tip. The upper graph shows the x tip position and the lower graph shows the y position. The EKO has a faster response to the target profile than OL.

For the OL measurement, we see that the model generally over-estimates tip movement resulting in a smaller amplitude than desired, especially for the vertical axis. The RMS errors for the y axis are larger that those of the x axis. Given the forces and weight of the tip, it is unlikely that gravity has a substantial influence here. The most likely explanation for difference between axis is an unequal pretension between the two instrument motors. Using EKO, we find that the tracking performance is improved over OL, but the shape does not closely resemble a circle. In figure 2 we can see that EKO speeds up the response over OL, and improves the amplitude mismatch for the y axis. EKO reduces the mean RMS error by 43% and 39% for x and y, respectively.

B. Square

Figure 3 shows the plot of the tip position in the ultrasound image plane. Figure 4 shows the X and Y positions individually. Table II shows the RMS errors of the measurement for this target profile.

From the OL graph in figure 3 we see that the square is tilted. A reason for this could be that the tendons are not aligned with the ultrasound probe. Another explanation for

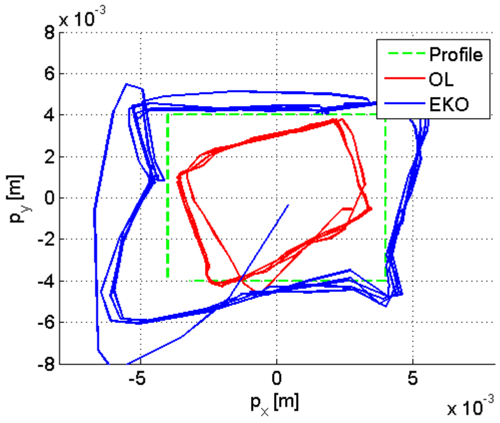

Fig. 3. XY plot of the tip position in the ultrasound image plane. Five cycles are shown for both controllers. The square shapes for both OL and EKO are tilted. The OL controller generally does not reach the desired amplitude, the EKO's amplitude is too large.

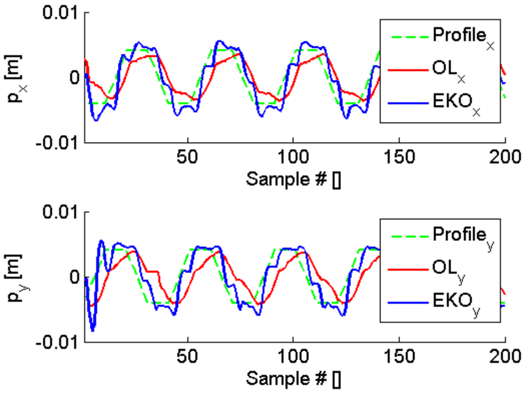

Fig. 4. Horizontal and vertical positions of the tip. The upper graph shows the x tip position and the lower graph shows the y position. For the y-axis, the EKO has a faster response to the target profile than OL. The EKO initially suffers from overshoot in y direction.

	RMS errors			
	OL x[mm]	OL y[mm]	EKO x[mm]	EKO y[mm]
Cycle 1	2.84	3.48	2.10	2.75
Cycle 2	2.45	3.28	1.80	1.87
Cycle 3	2.45	3.27	1.82	1.87
Cycle 4	2.44	3.25	1.88	1.86
Cycle 5	2.45	3.25	1.78	1.85
Mean	2.53	3.30	1.87	2.04
σ	0.16	0.09	0.12	0.36

TABLE II

Controller Evaluation: Square. The EKO improves performance of OL by 26% and 38 % for x and y direction, respectively. The EKO's overshoot in y direction shows up with a higher RMS error for the first cycle.

a rotated shape is asymmetrical 'crosstalk' between the two tendon pairs; i.e. movement in one tendon pair influences the other tendon pair. In case the instrument is merely rotated one expects the resulting graph to be merely rotated as well. However, we find that the horizontal edges of the square are not parallel. This may again indicate crosstalk, and/or it indicates asymmetry between positive and negative motion for the horizontal axis. Observing the behaviour of the tip for manual manipulation of the horizontal motor pulley confirmed the latter effect is present. The asymmetry between positive and negative motion is also observed when using EKO. At the positive horizontal edge the EKO is able to trace a horizontal straight line, but at the negative horizontal edge it is not able. The shape however resembles much more of a square than the OL shape, so EKO is able to partly overcome the model mismatch. EKO improves the RMS errors of EL by 26% and 38 % for x and y direction, respectively. In both OL and EKO, we see a significant start-up effect; the first cycle has higher RMS errors, especially for EKO in y direction. This also causes the standard deviation of EKO y direction to stand out. EKO overshoots for some time after start-up, which can be seen in both the XY plot as the p_y plot. The EKO estimate suffers from a large initial error. Providing a model with dynamics enables the EKO's filter functionality and will improve the robustness to these situations.

C. *Figure 8*

Figure 5 shows the plot of the tip position in the ultrasound image plane. Figure 6 shows the X and Y positions individually. Table III shows the RMS errors of the measurement for this target profile.

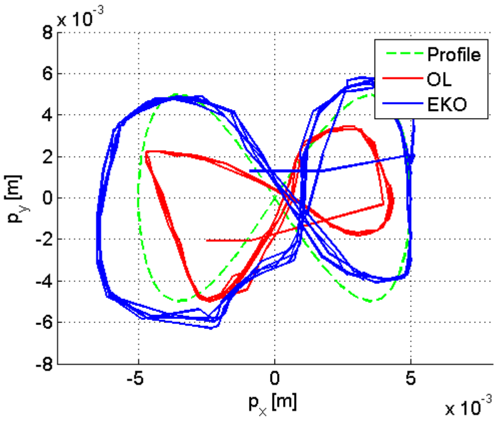

Fig. 5. XY plot of the tip position in the ultrasound image plane. Five cycles are shown for both controllers. The shapes for both OL and EKO are tilted. The EKO under-estimates the position for negative y motion, causing a larger amplitude.

The first thing to notice in 5 is that OL may have hit a mechanical limitation in the left of the image. Please remember that the offset is subtracted from measurement; the EKO measurement may not have that problem although the (offset compensated) amplitude is higher than that of OL. As with the square motion profile, we see that the shape is tilted. And, as before, we see an asymmetry for the horizontal axis; both OL and EKO have larger amplitudes at the negative side than the positive side. Asymmetry for the vertical axis is only observed in figure 6 for OL, where the downwards slope seems to be more problematic than the upwards edge. Again, both controllers suffer from larger errors in the first cycle. This is due to the profile starting from positions unequal to the origin. The EKO improves the accuracy of OL by 27% and 38% for x and y, respectively.

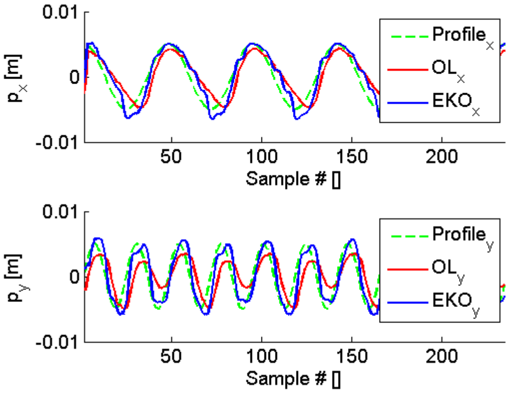

Fig. 6. Horizontal and vertical positions of the tip. The upper graph shows the x tip position and the lower graph shows the y position.

	RMS errors			
	OL x[mm]	OL y[mm]	EKO x[mm]	EKO y[mm]
Cycle 1	2.45	3.09	1.77	1.92
Cycle 2	1.99	3.07	1.46	1.92
Cycle 3	2.00	3.08	1.46	1.91
Cycle 4	2.00	3.07	1.45	1.94
Cycle 5	2.00	3.10	1.44	1.95
Mean	2.09	3.08	1.52	1.93
σ	0.18	0.01	0.13	0.02

TABLE III

CONTROLLER EVALUATION: FIGURE 8. THE EKO IMPROVES THE OL BY 27% AND 38% FOR x AND y, RESPECTIVELY.

IV. CONTROLLER WITH HYSTERESIS COMPENSATION RESULTS

The differences between Open-loop with Hysteresis Compensation (OL+HC) control and Extended Kalman Observer with Hysteresis Compensation (EKO+HC) control were investigated. These measurements are performed to evaluate the performance of the controller using (a non-optimal) hysteresis compensator. Each target profile is treated separately.

A. *Circle*

Figure 7 shows the plot of the tip position in the ultrasound image plane. Figure 8 shows the X and Y positions individually. Table IV shows the RMS errors of the measurement for this target profile.

The RMS errors of the OL+HC measurement have decreased comparing to OL measurements, see tables IV and I. OL+HC improves the accuracy over OL by 31% and 11% for horizontal and vertical motion, respectively. The EKO+HC result on the other hand looks over-aggressive.

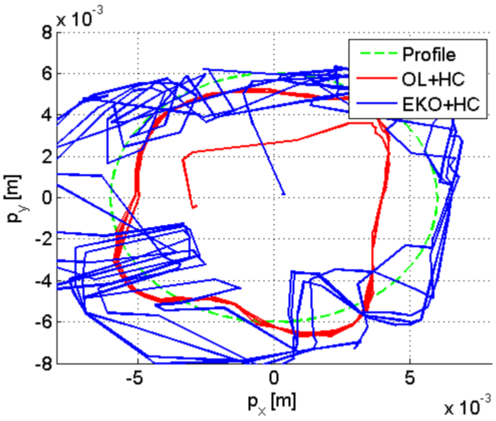

Fig. 7. XY plot of the tip position in the ultrasound image plane. Five cycles are shown for both controllers. The EKO overshoots the desired profile.

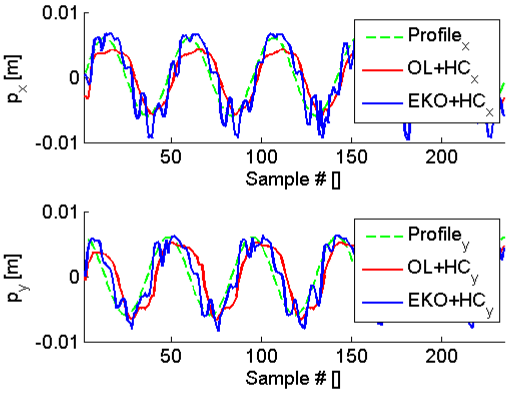

Fig. 8. Horizontal and vertical positions of the tip. The upper graph shows the x tip position and the lower graph shows the y position. The EKO overshoots the profile for both the x and y axis.

	RMS errors			
	OL+HC x [mm]	OL+HC y [mm]	EKO+HC x [mm]	EKO+HC y [mm]
Cycle 1	2.43	3.43	2.16	2.31
Cycle 2	2.25	3.34	2.14	1.99
Cycle 3	2.24	3.25	1.97	2.26
Cycle 4	2.25	3.27	2.34	1.74
Cycle 5	2.25	3.24	2.32	2.16
Mean	2.28	3.31	2.18	2.09
σ	0.07	0.07	0.13	0.21

TABLE IV

CONTROLLER & HC EVALUATION: CIRCLE. ALTHOUGH STANDARD DEVIATIONS ARE HIGHER FOR EKO+HC, IT IMPROVES OL+HC BY 4% AND 37% FOR x AND y, RESPECTIVELY

Figure 8 shows significant overshoot behaviour. Note that at every direction change (downwards/upwards) the hysteresis compensation becomes active and attempts to cross the hysteresis width in one action. This may cause the (weakened due to lacking model dynamics) EKO to overcompensate the model mismatch. The EKO+HC x and y positions do not show a strong repetitive behaviour, which also shows up in an increased standard deviation. Although the result of EKO+HC appears noisy, it still improves over OL+HC by 4% and 37% for x and y, respectively.

B. Square

Figure 9 shows the plot of the tip position in the ultrasound image plane. Figure 10 shows the X and Y positions individually. Table V shows the RMS errors of the measurement for this target profile.

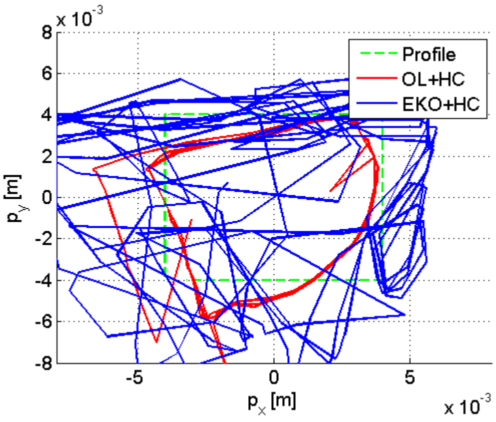

Fig. 9. XY plot of the tip position in the ultrasound image plane. Five cycles are shown for both controllers. The square shape is hard to distinguish for the EKO because of overcompensating.

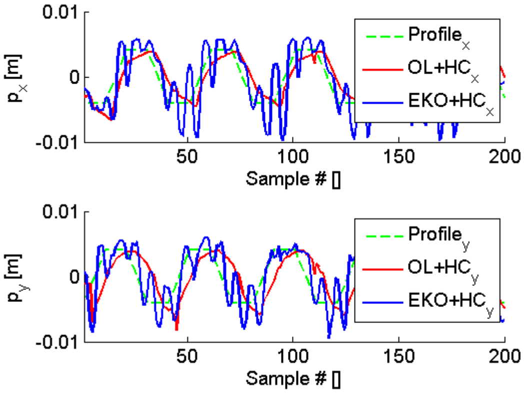

Fig. 10. Horizontal and vertical positions of the tip. The upper graph shows the x tip position and the lower graph shows the y position. The EKO overshoots the profile for both the x and y axis.

The same effects occur for the square motion profile as the circle motion profile. Comparing table V to table II, OL+HC improves the accuracy over OL by 22% for horizontal motion, although OL+HC is 2% less accurate

	RMS errors			
	OL+HC x [mm]	OL+HC y [mm]	EKO+HC x [mm]	EKO+HC y [mm]
Cycle 1	2.24	3.42	2.48	3.26
Cycle 1	1.93	3.46	3.51	2.83
Cycle 1	1.93	3.28	3.59	2.55
Cycle 1	1.91	3.34	3.85	2.50
Cycle 1	1.88	3.32	3.56	2.68
Mean	1.98	3.37	3.40	2.76
σ	0.13	0.07	0.47	0.27

TABLE V

CONTROLLER & HC EVALUATION: SQUARE. EKO HAS HIGH STANDARD DEVIATIONS, BUT IMPROVES OL BY 22% FOR THE x AXIS, BUT IS 2% LESS ACCURATE FOR THE y AXIS.

than OL for vertical motion. The EKO overshoots, in figure 10 the intended edges are hardly visible, especially for p_x. Hence, the square shape is difficult to destinguish. Note that overshoot to negative horizontal motion is larger than overshoot to positive horizontal motion. This points to a faster tip response to negative, and hence an asymmetry in the instrument for horizontal axis. As with the circular motion profile the standard deviations for EKO are large, indicating non-deterministic behaviour.

C. Figure 8

Figure 11 shows the plot of the tip position in the ultrasound image plane. Figure 12 shows the X and Y positions individually. Table VI shows the RMS errors of the measurement for this target profile.

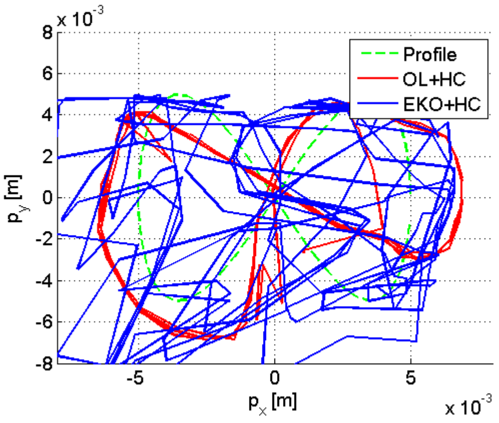

Fig. 11. XY plot of the tip position in the ultrasound image plane. Five cycles are shown for both controllers. The figure 8 shape is hard to distinguish for the EKO because of overcompensating.

OL+HC shows improvement over OL by 14% for the horizontal axis. The vertical axis however shows a 18% decrease of accuracy with OL+HC. The EKO+HC algorithm shows the same issues as with the other motion profiles. Overshoot and aggressive reaction to model mismatch are visible in figure 12. Nondeterministic behaviour also shows up in that figure and in large standard deviations.

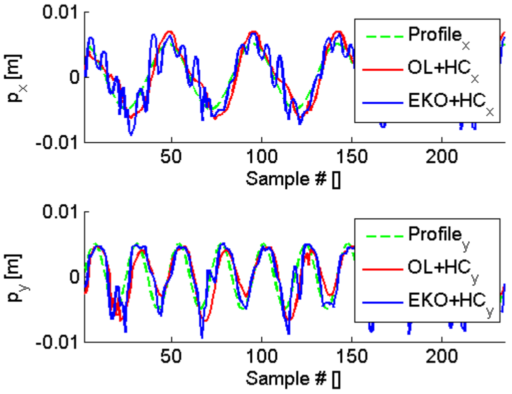

Fig. 12. Horizontal and vertical positions of the tip. The upper graph shows the x tip position and the lower graph shows the y position. Overcompensating is visible for the EKO for both axis.

	RMS errors			
	OL+HC x [mm]	OL+HC y [mm]	EKO+HC x [mm]	EKO+HC y [mm]
Cycle 1	1.96	2.69	2.69	2.31
Cycle 2	1.75	2.57	1.77	1.94
Cycle 3	1.70	2.56	1.92	2.23
Cycle 4	1.77	2.60	2.15	2.24
Cycle 5	1.78	2.56	2.42	3.12
Mean	1.79	2.60	2.19	2.37
σ	0.09	0.05	0.33	0.40

TABLE VI

CONTROLLER & HC EVALUATION: FIGURE 8. EKO HAS HIGH STANDARD DEVIATIONS, AND DOES NOT SIGNIFICANTLY IMPROVE ACCURACY OVER OL.

REFERENCES

[1] W. Lindh, M. Pooler, C. Tamparo, and J. Cerrato, *Delmar's Comprehensive Medical Assisting Administrative and Clinical Competencies*. Medical Assisting, Cengage Learning, 1997.

[2] P. Haouzi, N. Ahmadpour, H. J. Bell, S. Artman, J. Banchs, S. Samii, M. Gonzalez, and K. Gleeson, "Breathing patterns during cardiac arrest," *Journal of Applied Physiology*, vol. 109, no. 2, pp. 405–411, 2010.

[3] V. Duindam and S. Sastry, "Geometric motion estimation and control for robotic-assisted beating-heart surgery," in *IROS, 2007*, pp. 871–876, 2007.

Conclusions

This section will review the achieved results and experimental measurements in this thesis and draw conclusions.

PLATINUM

An experimental setup was designed and built that holds and controls a prototype minimally invasive surgical instrument, while ultrasound images of the instrument's tip can be recorded. The chosen mechanical and electrical concepts are demonstrated to be functional.

Modelling

A forward model for describing the relation of motor angles to tip position was composed. An inverse model algorithm, describing the relation of tip position to motor angles was designed and constructed. No dynamics were included in the model, which reduced some terms of the Kalman equations, and hence caused limited filter capabilities of the Kalman observer.

Hysteresis & Hysteresis Compensation

Hysteresis was found present in the system. Some possible causes for this effect are identified, however no single root cause was found. The hysteresis is likely the result of multiple causes. From identification measurements we conclude that hysteresis in the system is no pure mechanical dead-zone.

Hysteresis reduction was attempted, however it was found that the hysteresis loop shows asymmetry. An asymmetrical loop causes hysteresis reduction algorithms to drift. Classical hysteresis compensation was successfully measured, reducing the observed hysteresis by 53% and 51% for the horizontal and vertical axis, respectively. Possible reasons for not completely compensating the hysteresis are under-estimation of parameters and delay influences.

Controller evaluation

A delay of about 0.8 seconds was found in the path from tip motion to measurement feedback in the controller. This delay causes over-aggressive compensation behaviour for closed-loop systems like Internal Model Control and the Extended Kalman Observer. Controller evaluation measurements were performed using slower controller rates to minimize its effects.

Open-loop (OL) versus Extended Kalman Observer (EKO) experiments were performed, where the EKO improved accuracy of the horizontal tip position over OL by 43%, 26% and 27% for circle, square and figure 8 motion profiles, respectively. The EKO improved over OL for the vertical tip position by 39%, 38% and 38% for circle, square and figure 8 motion profiles, respectively.

It was observed that the functionality of the EKO is limited due to the absence of dynamics in the model, since the filtering function of any Kalman observer depends on the presence of dynamics. These limitations were visible when combining the controllers with hysteresis compensation. The EKO with hysteresis compensation is overcompensating for model mismatch. The hysteresis compensation is causing rapid changes in actuator position, creating a noisy difference signal. The combination of delay, absence of model dynamics and classic hysteresis compensation are causing the EKO controller to overcompensate.

Recommendations and Future Work

During the research of this project a number of issues were found which can be improved and require investigation in future studies. Some solutions and/or recommendations to improve these issues will be presented, together with general ideas to improve the hardware or software of the experimental setup, the instrument, model and controllers.

PLATINUM

For PLATINUM, some improvements are possible:

- Friction can be reduced by choosing smaller bends in the Bowden assemblies. It turns out that the motor pulleys need not to be serviced often, since the current design of the pulleys is proven to be robust. In the near future it is expected that the pretension mechanisms will have to be serviced more often. Reducing friction and improving pretension serviceability can be done by reducing the motor angles (i.e. the angle between longitudinal axis of the motors will go towards 180 degrees). This will reduce the bend in the Bowden sleeves and hence reduce friction. The reduced angle improves pretension serviceability because there is more space to provide a pretension force.
- The interface between water tank and instrument should be replaced by a redesign. With the interface design currently fitted to the setup it is difficult to push the instrument through the o-rings. A redesign was made and prototypes were printed. The redesign solves the problems passing the instrument trough the o-rings.
- The interface between water tank and instrument is made of 3D printed plastic. Although functional in this project, the durability of the interface may be improved by selecting other materials (e.g. durable plastic or corrosion-free metal).

Towards clinical environments

Locating the instrument tip using 2D ultrasound is difficult, in the future the 2D ultrasound needs to be replaced by 3D ultrasound. This reduces the chance of the instrument tip being not visible in the ultrasound image and increases its usability in a clinical environment.

Delay

The effect that limits the performance of the system the most is delay, found in the path from tip movement to controller measurement inputs. Delay can never be completely eliminated, but efforts can be made to reduce it. In order to reduce delay, some components of the system can be integrated. Different levels of integration are possible:

1. Integrate s-video image capturing in the PC. The image capturing device was estimated to have about 0.4 seconds delay. If image capturing is integrated on e.g. a PCI card in the PC, this delay can be reduced.

2. Use the (RGB) monitor output of the ultrasound machine to capture images (instead of the S-video connection). This improves resolution and probably increases capture frequency.
3. Eliminate analogue images. The Ultrasound machine has a LAN connection, and probably there is a possibility to transmit digital images over the network to the PC. This eliminates digital-to-analog and analog-to-digital conversion times, reduces noise, increases resolution and increases capture frequency.
4. The PC is eliminated and all image processing and control actions are moved to the ultrasound machine (possibly using PCI cards). This is a completely integrated system where the only interfaces out of the ultrasound machine are the probe and device control signals.

In the current state of development, it is recommended to skip the options 1 and 2 and implement option 3. Options 1 and 2 solve delay to some extend, but option 3 likely has the most benefits with limited effort to implement. The completely integrated system of option 4 is impossible without dedicated effort from the ultrasound machine manufacturer.

Controller

It is recommended to include dynamic behaviour in the instrument model. This will improve modelling accuracy, but more importantly it will enable the filtering function of EKO. Especially when EKO was combined with HC, overcompensation to model mismatch was observed. This is likely due to difference signals spiking. Allowing EKO to filter will reduce the aggressive compensation behaviour.

Another option to reduce overcompensation, in case dynamics in the model are considered undesired or superfluous, is to manually filter the set-points and measurements while the controller frequency is increased. The effective controller response time stays the same, but the signals will be more fluent and thus difference signals will be less noisy.

Instrument tip behaviour

Hysteresis was found present in the system, some identification hereof is performed. However, the behaviour of the instrument and setup is not completely understood yet. Follow-up research is recommended to include:

- A closer look at hysteresis, investigate which of the causes affect hysteresis most. It is known that the hysteresis is not pure backlash, but any other effects have not yet been found. Investigate possible velocity dependant hysteresis loop width, and possible other effects that may affect hysteresis loop width.
- Elaborate research of tip behaviour, specifically for this instrument construction. Measurements have shown signs of: crosstalk between the two tendon pairs, asymmetry of the instrument for positive versus negative motion. The effect of pretension on measurements has not been investigated, it is recommended that future studies will focus on this.

Appendix A: PLATINUM Mechanics

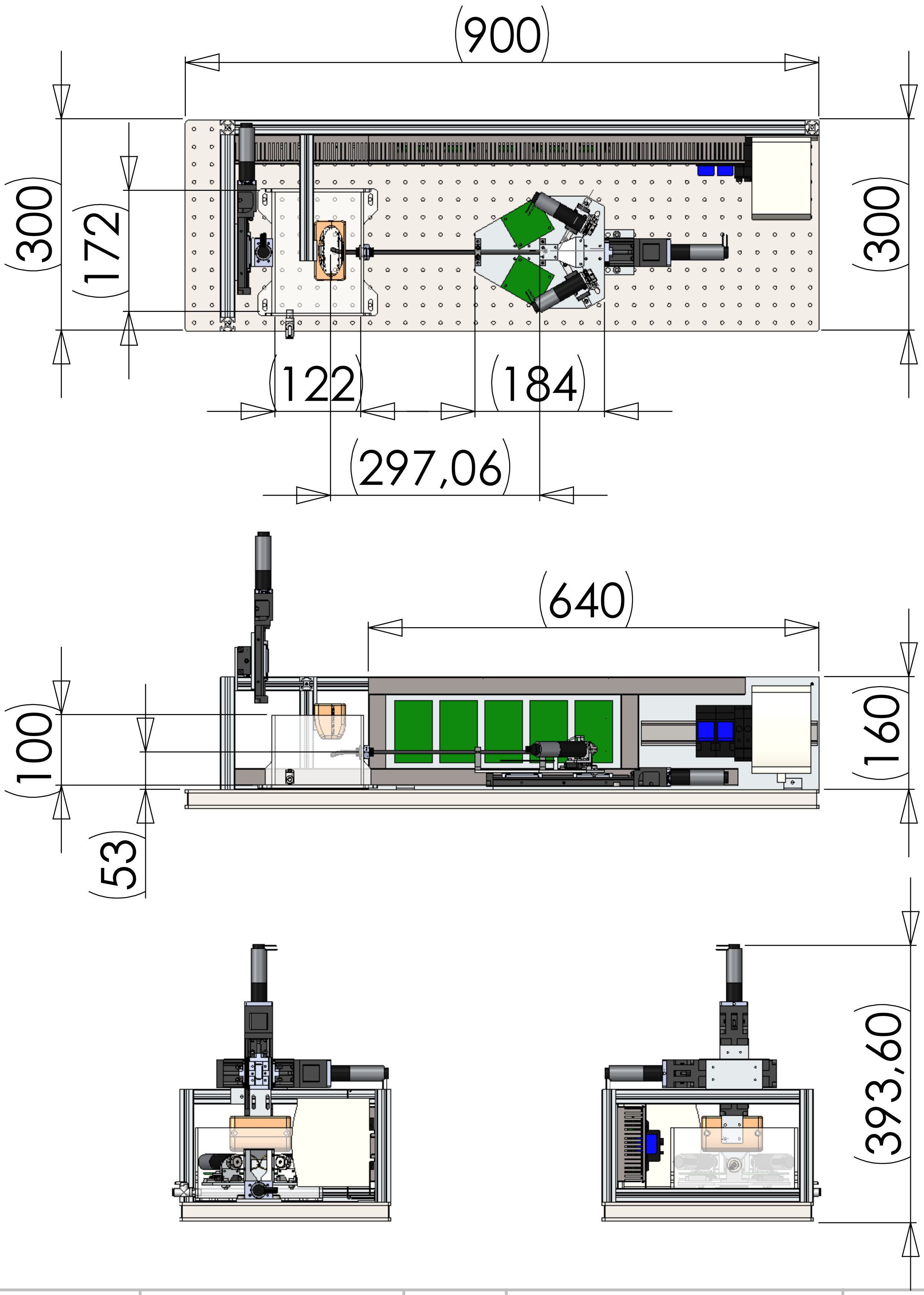

UNLESS OTHERWISE SPECIFIED:
DIMENSIONS ARE IN MILLIMETERS
SURFACE FINISH:
TOLERANCES:
LINEAR:
ANGULAR:

FINISH:

DEBUR AND
BREAK SHARP
EDGES

DO NOT SCALE DRAWING

REVISION

	NAME	SIGNATURE	DATE
DRAWN			
CHK'D			
APPV'D			
MFG			
Q.A			

TITLE:

MATERIAL:

WEIGHT:

DWG NO.

SetupAssembly

A4

SCALE:1:8

SHEET 1 OF 1

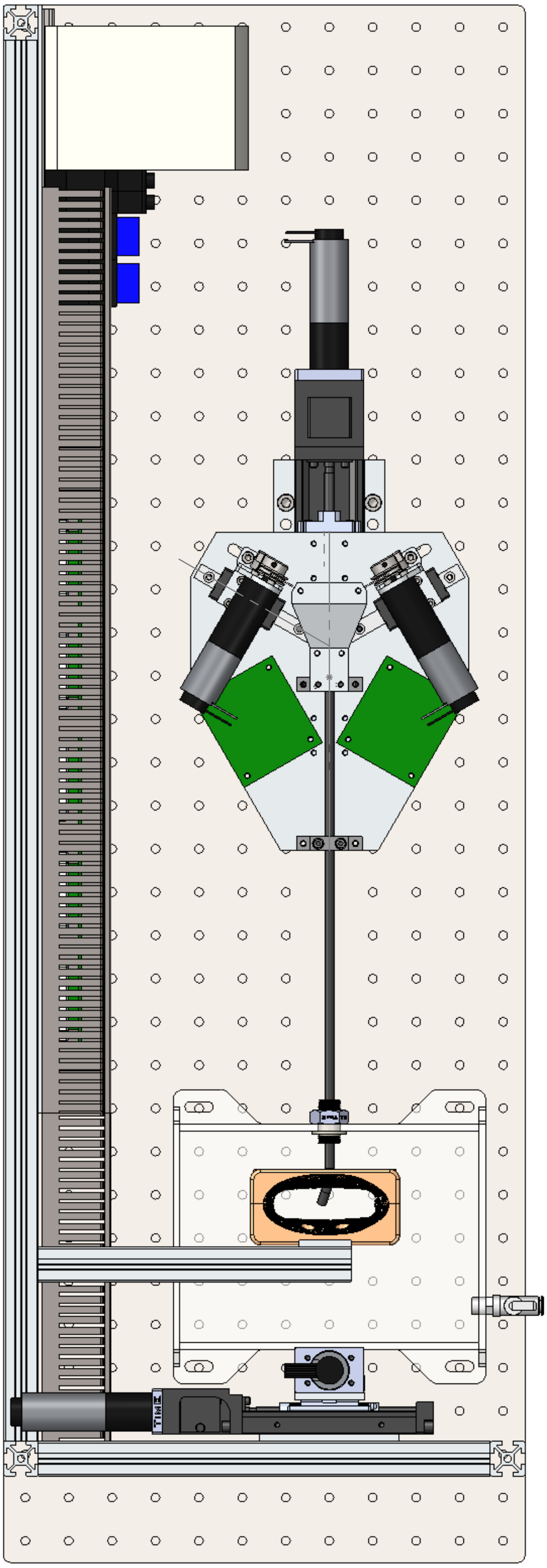

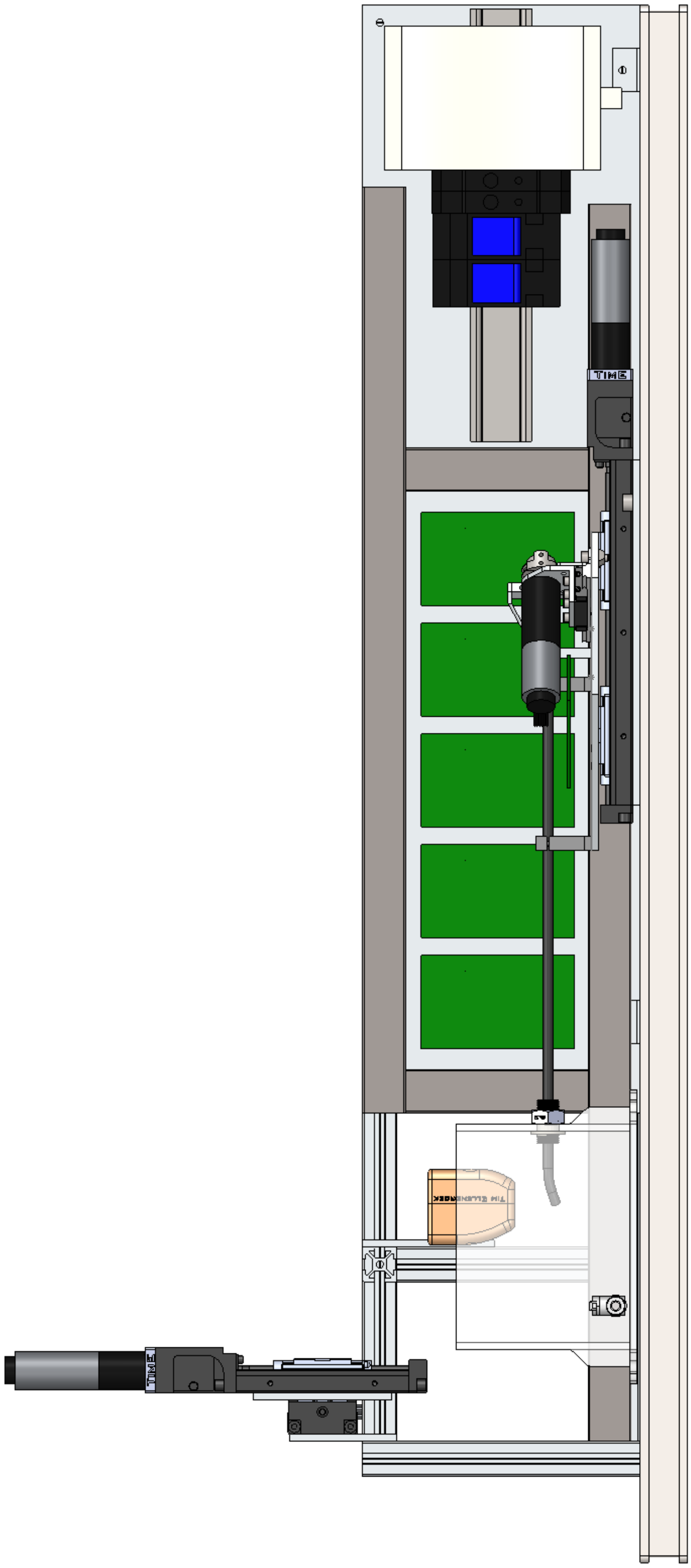
TIME
TIME

Appendix B: PLATINUM Electrics

Elmo Motorcontrollers

There are 5 Elmo Whistle 2.5/60 motor controllers mounted in the setup. Table 1 presents their settings.

Function	Environment Vertical	Environment Horizontal	Instrument Horizontal	Instrument Vertical	Instrument Z
Number	5	4	3	2	1
Motor power	25W	25W	12W	12W	25W
End-switch 1	Near-side	Near-side	-	-	Near-side
End-switch 2	Far-side	Far-side	-	-	Far-side
Direction definition	Negative	Negative	Negative	Positive	Negative
CAN ID	45	44	43	42	41
Positive motion	To far	To far	Tip to right	Tip to up	To far

Table 1: Elmo configuration.

Appendix C: Software

Control assignments and measurements on the motors of PLATINUM are relative to the initial position. For software to obtain an absolute position, a homing procedure is designed. The homing listing is shown in algorithm 1.

Algorithm 1 Homing procedure

```
Move $z$ motor to far end-stop
Record position of instrument shaft:
while No lock on device centroid do
    ▷ Wait for lock
end while
$\mathbf{p_0} = average(\#samples)$
Reset $z$ encoder
Align tip with ultrasound plane:
while $\bar{\mathbf{p}} \neq \mathbf{p_0}$ do
    $\theta_{h,k} = \theta_{h,k-1} + Gain \cdot (\bar{\mathbf{p}}_\mathbf{h} - \mathbf{p}_{\mathbf{0},\mathbf{h}})$
    $\theta_{v,k} = \theta_{v,k-1} + Gain \cdot (\bar{\mathbf{p}}_\mathbf{v} - \mathbf{p}_{\mathbf{0},\mathbf{v}})$
end while
Reset $\theta_h$, $\theta_v$ encoders
```

First, the instrument shaft is positioned in the ultrasound plane, and its zero position is recorded. Then the tip is aligned with the shaft to ensure the instrument is straight after homing. Finally, the encoders are reset.

References

[1] M. F. Newman, J. L. Kirchner, B. Phillips-Bute, V. Gaver, H. Grocott, R. H. Jones, D. B. Mark, J. G. Reves, and J. A. Blumenthal, "Longitudinal assessment of neurocognitive function after coronary-artery bypass surgery," *New England Journal of Medicine*, vol. 344, no. 6, pp. 395–402, 2001. PMID: 11172175.

[2] P. Haouzi, N. Ahmadpour, H. J. Bell, S. Artman, J. Banchs, S. Samii, M. Gonzalez, and K. Gleeson, "Breathing patterns during cardiac arrest," *Journal of Applied Physiology*, vol. 109, no. 2, pp. 405–411, 2010.

[3] S. B. Kesner and R. D. Howe, "Position control of motion compensation cardiac catheters.," *IEEE Transactions on Robotics*, vol. 27, no. 6, pp. 1045–1055, 2011.